Investigation and Optimization of a High Voltage Piezoelectric Particle Accelerator

---

A Thesis
presented to
the Faculty of the Graduate School
at the University of Missouri

In Partial Fulfillment
of the Requirements for the Degree
of Master of Electrical Engineering

---

by

Brady B. Gall

Dr. Scott Kovaleski, Thesis Supervisor

July 2012

The undersigned, appointed by the Dean of the Graduate School, have examined the thesis entitled:

Investigation and Optimization of
a High Voltage Piezoelectric
Particle Accelerator

presented by Brady B. Gall
a candidate for the degree of Master of Electrical Engineering
and hereby certify that in their opinion it is worthy of acceptance.

Dr. Scott Kovaleski

Dr. Jae Kwon

Dr. William Miller

Acknowledgements

First, I would like to thank Dr. Kovaleski for your academic and professional guidance throughout my graduate education. Thank you for providing me with the time, energy, and resources necessary to cultivate my scientific curiosity. Your instruction has shaped my growth as a student and as a researcher.

Thank you to my fellow students and colleagues for your camaraderie and advice. A special thank you Brian Hutsel for being a true friend and making my graduate experience one of the most enriching and fun periods of my life. Thank you James VanGordon and Peter Norgard for always pushing me to do my best. Thanks to Emily Baxter, Erik Becker, Karl Olson, Alec Hughs, and David Rice for your friendship and support.

Finally, thank you to my mother, Jan Gall, for raising me with the values and work ethic necessary to succeed in both science and in life. You have always taught me the importance of hard work and positive thinking and my success is a direct result of your diligence and compassion. I have never questioned your presence in my life as a source of love, support, and motivation, and I couldn't be more proud to be your son.

Contents

List of Tables

List of Figures

Chapter 1

Introduction

1.1 Thesis Overview

Large, high-power technologies such as linear accelerators, synchrotrons, and free electron lasers are commonly used to drive x-ray sources for scientific and medical applications [1]. Micro/nano systems (MEMS) are an emerging field which, due to weight, size, and power constraints, have limited compatibility with traditional x-ray sources. Despite these limitations, x-ray applications such as lithography, tomography, and radiography are appealing for MEMS research [2–4]. Advancements in compact high voltage generation using phenomena such as the pyroelectric and triboelectric effects offer promise for MEMS x-ray sources [5–7]. The piezoelectric effect is another phenomenon which can be used as a method for compact high voltage x-ray generation [8–10].

The piezoelectric effect is commonly used to produce high voltage in commercial applications such as LCD backlights, gas-discharge lamp ignitors, and compact AC/DC converters [11]. The output voltage of these applications is between $30-300$ V [12–14]. Experimental applications of the piezoelectric effect often operate at increased voltages, such as a dielectric plasma reactor at 5 kV output [15]. However, x-ray sources typically require between $40-60$ kV to be useful in imaging applications, such as tomography [3]. Considering that x-ray sources operate at much higher voltages than typical piezoelectric devices, a piezoelectric source must be highly optimized to become viable for x-ray production. The advantages of piezoelectric materials, including low weight, low power, high efficiency, and high gain [11], have motivated investigation of the piezoelectric effect for compact x-ray applications [9, 10].

This thesis contains analysis of the piezoelectric effect as a means to produce high voltage. The goal of this analysis is to determine if piezoelectric transformers can be used effectively in compact x-ray source applications. For the piezoelectric effect to be considered a viable mechanism for x-ray sources, the piezoelectric device must be able to produce x-ray energies ranging between $40-60\,\mathrm{keV}$. This chapter discusses the background theory for the thesis. First, the theory of piezoelectric devices as high gain voltage transformers is discussed. The next section discusses the physics of the x-ray source that was coupled to the high voltage piezoelectric transformer. Lastly, a discussion of neutron physics proposes additional applications of the high voltage piezoelectric source.

Chapter 2 discusses the modeling techniques used to simulate the piezoelectric voltage transformer. A piezoelectric model is used to investigate the relationship between the voltage and stress of the transformer, establishing operating conditions which maximize output voltage while minimizing the risk of fracturing the piezoelectric crystal. An electrostatic model is used to design charged particle optics which increase the electron beam flux on a bremsstrahlung target.

Chapter 3 discusses the experimental configurations and diagnostics used to test the output characteristics of a piezoelectric transformer x-ray source. Initially, the x-ray production method is tested. Subsequent configurations are optimized to increase x-ray flux of the transformer source. A piezoelectric plasma generator configuration is introduced as an alternative method for reaching high voltage and producing x-rays.

Chapter 4 presents the experimental results of the investigation. Initial experiments verified that the piezoelectric x-ray source was capable of producing x-rays. Improvements in diagnostics, analysis techniques, and experimental configurations successfully and repeatedly demonstrated x-ray energies greater than 100 keV. Additionally, the plasma generator demonstrated that piezoelectric transformers can be used to produce rf capacitive discharges at pressures between 10−25 mTorr and was capable of producing x-rays at 9 mTorr.

Lastly, Chapter 5 summarizes the work and results presented in the thesis. An analysis of the piezoelectric x-ray source discusses the experimental configurations used to produce x-rays and the improvements made to these methods. This analysis provides a possible direction for future work on the piezoelectric high voltage source for both x-ray and neutron applications.

1.2 Piezoelectric Transformer

The piezoelectric effect is governed by two coupled equations that combine the Hooke's Law relationship between stress and strain and the constitutive relationship between electric field and electric displacement. These equations are shown in eqs. 1.1 and 1.2 [16].

$$\{S\} = [s^E]\{T\} + [d^t]\{E\} \tag{1.1}$$

$$\{D\} = [d]\{T\} + [\varepsilon^T]\{E\} \tag{1.2}$$

The variables S, T, E, and D are strain, stress, electric field, and electric displacement. The constants s^E, d^t, d, and ε^T are tensors representing the elasticity, indirect piezoelectric coupling coefficient, direct piezoelectric coupling coefficient, and permittivity. Due to the anisotropic nature of many piezoelectric materials, these tensors can have different values in each of the geometric directions. This anisotropic property can be used to increase the voltage of an applied AC signal [17].

Figure 1.1 shows an electroded piezoelectric material in the shape of a flat bar. The geometry is known as the Rosen transformer [18–20], and is shown in with primary geometric axes x_1, x_2, and x_3.

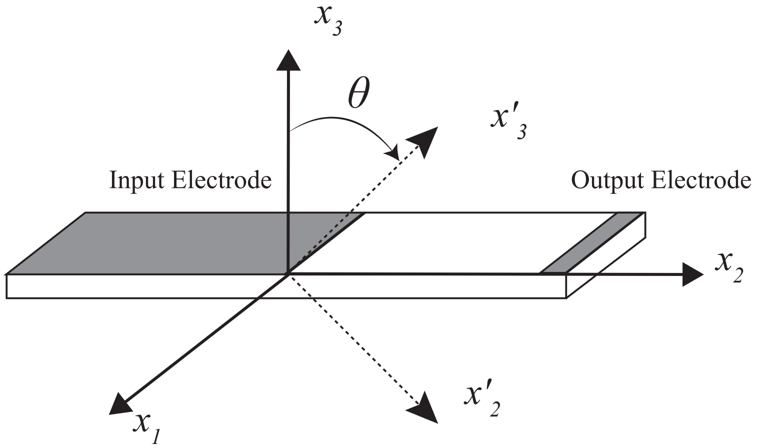

Figure 1.1: Bar-shaped piezoelectric transformer with rotated crystallographic orientiation and input electrodes (obverse electrode not visible).

The Rosen transformer in Fig. 1.1 has an input and an output terminal used to deliver and extract energy, respectively. The input terminal is a pair of electrodes which span from the extremity of the transformer to the center in the x_2 direction. The electrodes are patterned opposite to one another on the surfaces normal to the x_3 direction, shown as a grey region on the left side of the transformer. The output terminal is a single electrode, shown on the right side of the transformer in Fig. 1.1. This electrode is approximately 5 % the length of the transformer in the x_2 direction and is located at the extremity of the bar.

To operate the transformer, a low amplitude ($\sim 10\,\mathrm{V}$) AC voltage is applied to the input electrodes of the transformer. Electric fields in the x_3 direction couple into mechanical displacements in the x_2 direction and an output voltage is produced at the extremity of the bar. This is known as the length extensional mode [18]. The piezoelectric transformer should be driven at or near its natural mechanical resonance to operate in the length extensional mode. The resonant frequency ω_n is determined by material properties and the dimensions of the bar, shown in Eq. 1.3 [9]. The variables l, s^E, and ρ are the length of the bar in the x_2 direction, the elasticity tensor, and the density of the material. The integer value n indicates the harmonic overtone.

$$\omega_n = \frac{n\pi}{l}\sqrt{\frac{s^E}{\rho}} \tag{1.3}$$

Lithium niobate was chosen as the material for the transformer in Fig. 1.1 because it has many favorable properties including low electric and elastic losses, high Q factor, and large piezoelectric coupling coefficients [17, 21]. Equation 1.4 shows that piezoelectric transformer has a large gain due to its geometry where L is length in the x_2 direction and T is thickness in the x_3 direction.

$$\begin{aligned} \tfrac{V_{out}}{V_{in}} &= k_{23}k_{33}Q\tfrac{L}{T} \\ k_{23} &= {}^{d_{23}}\!/\!\sqrt{s^E_{22}\varepsilon^T_{33}} \\ k_{33} &= {}^{d_{33}}\!/\!\sqrt{s^E_{33}\varepsilon^T_{33}} \end{aligned} \tag{1.4}$$

Lithium niobate has a high Q factor due to its low mechanical and electrical losses, which further increase the gain of the crystal. The piezoelectric coupling coefficients k_{23} and k_{33} are functions of the material properties of lithium niobate and the rotation angle of the bar, shown in Fig. 1.2 [17].

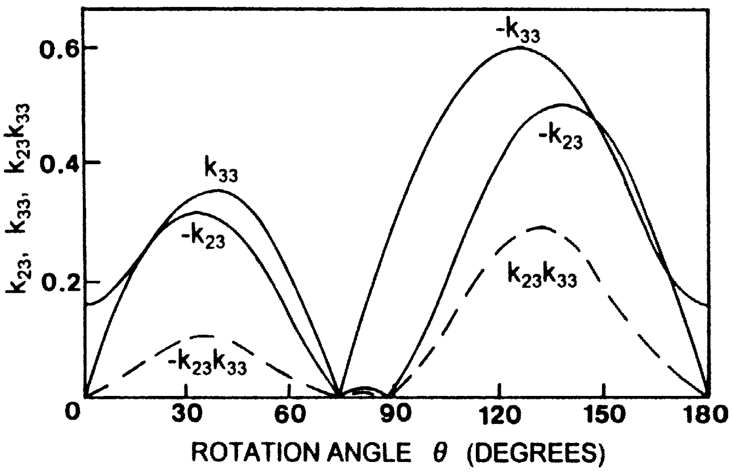

Figure 1.2: Piezoelectric coupling coefficients k_{23} and k_{33} and their product as a function of rotation angle [17].

Figure 1.2 shows that the coupling coefficients vary independently as a function of rotation angle. Rotation angle refers to angle between the primary axes of the bar and the crystallographic polarization of the lithium niobate lattice. The $k_{23}k_{33}$ product reaches a maximum at 135 degrees. This rotation is shown in Fig. 1.1 with the secondary axes x_2' and x_3' rotated by an angle θ about primary axis x_1. By increasing the $k_{23}k_{33}$ product, Eq. 1.4 shows that the voltage gain of the transformer increases.

The piezoelectric transformer is used to investigate the piezoelectric effect as a means to produce high voltage. Lithium niobate crystals with 135° rotation were manufactured for this experiment and electrodes were positioned in the Rosen geometry. AC voltage was applied to the transformer input to initiate length extensional resonance, producing high voltage at the output.

1.3 Piezoelectric X-ray Source Physics

Artificial x-ray sources can produce x-rays through two basic atomic mechanisms: x-ray fluorescence and bremsstrahlung radiation. In the case of x-ray fluorescence, an incident electron impacts an orbital electron of an atom, exciting it to a higher orbital energy. When the excited electron returns to its original orbital, the energy lost from this transition is given off as a characteristic x-ray. Bremsstrahlung radiation is given off by an incident electron as electrostatic forces from an atomic nucleus accelerate it, which causes it to emit an x-ray with energy equal to the energy lost from the acceleration [1]. In each case, a high energy electron is necessary to produce the x-ray. The high voltage piezoelectric x-ray source uses electron field emission structures to produce electrons which are accelerated into a target to produce bremsstrahlung x-rays.

Field emission is a quantum mechanical process in which electron charge is extracted from a material. Electric fields on the order of 10^6 V/cm are applied to the surface of a material, typically a metal. This high electric field deforms the potential barrier of the metal such that electrons near the Fermi level have a sufficiently high probability of tunneling out of the quantum well. This mechanism results in current densities on the order of many A/cm^2 [22, 23]. High electric fields are often achieved using field enhancement structures. An example of the field enhancement process is diagramed in Fig. 1.3 [24].

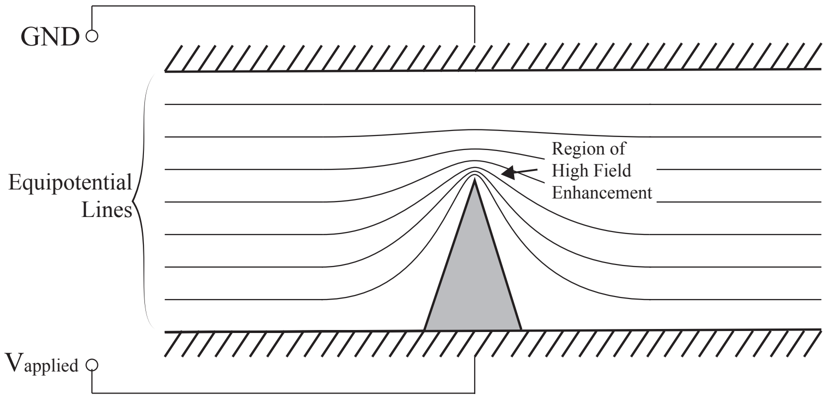

Figure 1.3: Diagram of a field enhancement structure compressing equipotential lines near its apex, producing a region of high electric fields for electron emission.

Figure 1.3 shows two electrodes with an applied voltage separated by a gap. A field enhancement structure on the energized electrode penetrates into the gap, compressing the equipotential lines at the tip of the structure, resulting in high local electric fields. The field enhancement factor is a ratio that describes the magnitude of the local electric field approximately 1 nm away from the tip surface to the total electric field across the gap. Equation 1.3 is used to calculate the field enhancement factor of an emitter [25].

$$\begin{aligned} F_m &= \tfrac{V}{d} \\ F_t &= V \cdot \gamma \\ \beta &= \tfrac{F_t}{F_m} \end{aligned} \tag{1.5}$$

The values F_m, F_t, V, and d are the electric field in the gap, the electric field 1 nm away from the emitter surface, the voltage across the gap, and the gap distance. The values γ and β are the geometric field factor and the field enhancement factor. The geometric field factor is a function of the shape and size of the emitter and typically ranges between 10^4 to 10^7 m^{-1} [26]. The output current of a field emitter is highly dependent on β, with higher values of β permitting higher current densities. The magnitude of β can be increased with various methods including increasing the height/base ratio of the emitter and producing extremely sharp emitter tips [27].

Field emission structures are used to extract electron beam current from the piezoelectric transformer. The emitters are platinum iridium wires that are adhered to the output terminal of the transformer. The energy of the emitted electrons in eV is equal to the electron charge multiplied by the output voltage of the transformer in V. Bremsstrahlung conversion is used to measure the energy of the emitted electrons, and subsequently, measure the output voltage of the transformer.

The bremsstrahlung phenomenon can be described by classical theory, which states that whenever a charge experiences an acceleration, it will radiate [28]. A diagram of the bremsstrahlung radiation process is shown in Fig. 1.4.

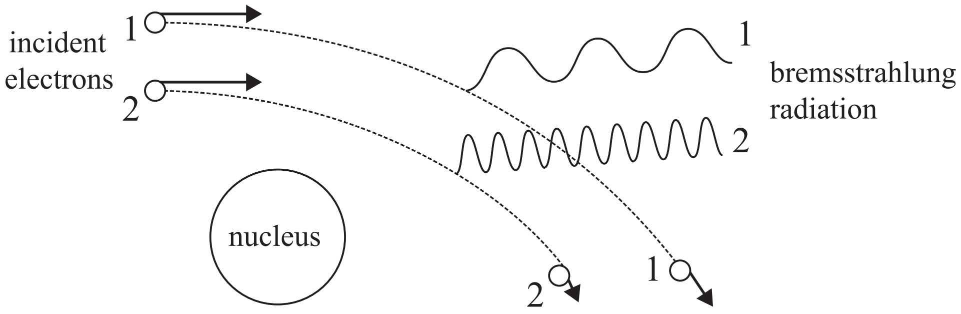

Figure 1.4: Diagram of the classical theory of bremsstrahlung radiation where electron energy is converted to a photon due to electrostatic acceleration.

In Fig. 1.4, two electrons of equal energy approach the vicinity of an atomic nucleus, with electron 1 farther away from the nucleus than electron 2. Both electrons are deflected by the electrostatic field of the nucleus and experience an acceleration due to this deflection. Two photons are produced by these deflections with the energy of each photon corresponding to the energy loss of each electron, respectively. This type of radiation is called bremsstrahlung radiation and is described by Duane and Hunt's law, shown in Eq. 1.6.

$$(h\nu)_{max} = T \tag{1.6}$$

Equation 1.6 states that a photon emitted by bremsstrahlung radiation can have maximum energy equal to the total kinetic energy of an incident electron, T. A beam of electrons will produce a spectrum of bremsstrahlung x-rays with energies ranging from 0 up to T. A voltage can therefore be indirectly inferred by sampling a bremsstrahlung spectrum and locating the maximum endpoint energy $h\nu$ of the spectrum. This is the method used to measure the output voltage of a piezoelectric transformer.

The intensity of bremsstrahlung radiation is proportional to the atomic number of the target material, as described in Eq. 1.7 [29].

$$I \propto a^2 \sim \frac{z^2 Z^2}{M} \tag{1.7}$$

The values I, a, z, Z, M are the emitted bremsstrahlung intensity, the acceleration of the incident particle, the charge of the incident particle, the atomic number of the target, and the mass of the incident particle, respectively. Equation 1.7 shows that bremsstrahlung intensity can be maximized by having a low mass projectile, such as an electron, incident on a high-Z target. Due to this relationship, electron beam targets used in the piezoelectric transformer experiments are high-Z metals such as iron (Z= 26) or tungsten (Z= 74).

1.4 Neutron Source Physics

In addition to compact x-ray applications, the piezoelectric transformer could also be a viable option for compact neutron production using the D(d,n)^{3}He nuclear reaction. In this reaction, an ionized deuteron, d, is accelerated into an idle deuterium atom, D, to produce a 2.45 MeV neutron, n, and an 820 keV helium isotope byproduct, ^{3}He [30]. The cross-section for the D(d,n)^{3}He reaction is strongly dependent on the energy of the projectile deuteron, as shown in Fig. 1.5 [31, 32].

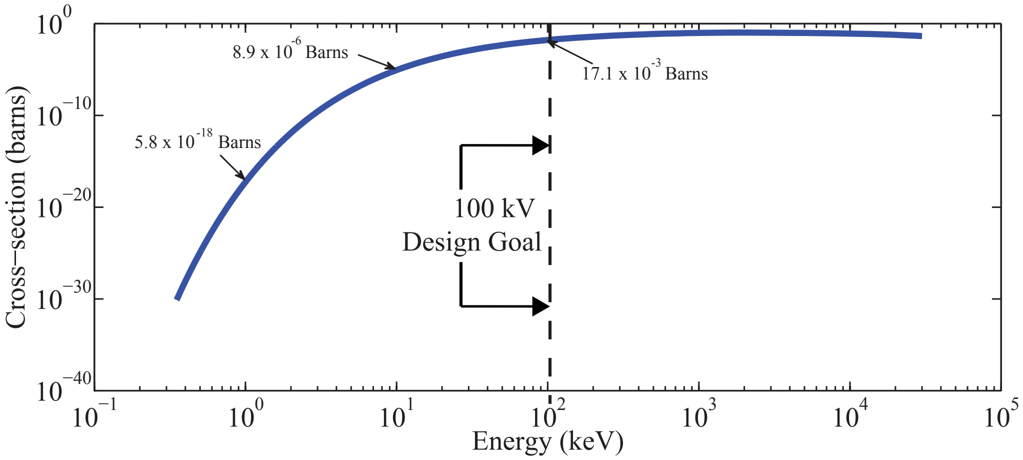

Figure 1.5: Cross-section for the D(d,n)^{3}He nuclear reaction as a function of deuteron energy

Figure 1.5 shows that the cross-section for the D(d,n)^{3}He reaction non-linearly increases with the energy of the deuteron. At 1 keV, the cross-section is 5.8×10^{-18} Barns, which increases to 8.9×10^{-6} Barns at 10 keV. At 100 keV, the cross-section reaches 17.1×10^{-3} Barns. As deuteron energy increases beyond 100 keV, a less substantial increase in cross-section occurs. This relationship between deuteron energy and cross-section indicates that an accelerator designed to cause the D(d,n)^{3}He reaction should be designed to reach at least 100 kV for a reasonable reaction cross-section. One application of a compact neutron source driven by a piezoelectric transformer is active interrogation.

Active interrogation is a technique to prevent the transportation of concealed nuclear materials such as uranium-235 [33–35]. Neutron radiation is often used in active interrogation because it can penetrate container walls and interact with the nuclear material, producing characteristic radiation in substantially larger quantities than the natural decay mechanisms alone. [36]. A diagram of the active interrogation process is shown in Fig. 1.6.

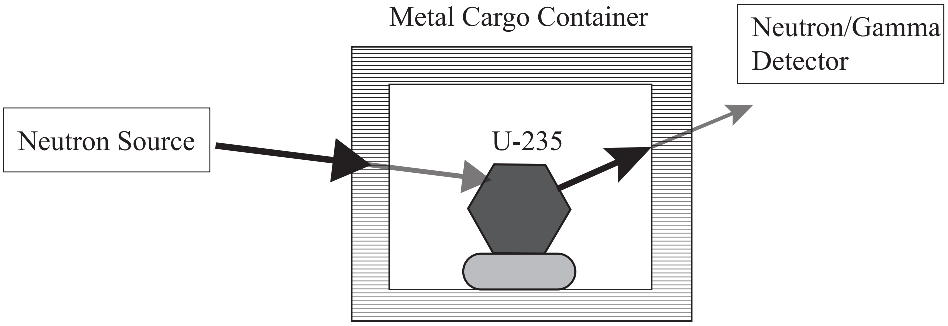

Figure 1.6: Diagram of active interrogation of concealed uranium-235.

Figure 1.6 shows a neutron source external to a concealed sample of uranium-235. Neutrons from this source can penetrate the walls of the container and interact with the uranium, resulting in characteristic nuclear reaction products. For example, when a fission event between a single neutron and an atom of uranium-235 occurs, up to 6 neutrons and up to 20 high energy gamma rays can be emitted. The gamma ray products have an energy of 300 keV or higher and can exit the container for external detection. The neutron products are particularly useful because they can cause further fission events in a chain reaction with the uranium, producing additional gamma ray and neutron products. [36, 37].

Active interrogation has been proposed for use in maritime and shipping settings where high volumes of metallic containers could presumably conceal the transportation of nuclear materials [38]. As a result, there is a demand for technologies that can permit the wide scale deployment of compact, low power, neutron sources for use in active interrogation applications [39]. While the voltage requirements for the piezoelectric transformer as a neutron source are substantially higher than those of the x-ray source, the benefits of such a compact neutron source do warrant investigation. This thesis contains experimental methods to investigate the limits of piezoelectric transformer output capabilities while considering both compact x-ray sources and neutron sources as possible applications for the piezoelectric effect.

Chapter 2

Modeling

2.1 Overview

This chapter discusses the modeling techniques and solutions that were used to support piezoelectric transformer experiments. All modeling was conducted in COMSOL Multiphysics, a finite-element analysis, solver, and simulation environment for physics and engineering applications [40]. It contains a suite of modules that can be used for solving specific physical problems. The structural mechanics and AC/DC modules was used to provide analysis for piezoelectric and electrostatic physics, respectively.

The model for the piezoelectric transformer is described in section 2.2. Initial conditions for the model and simulation methods are discussed. The results of the piezoelectric model are presented which demonstrate the electrical and mechanical parameters of a resonant piezoelectric crystal. The relationship between output voltage and von Mises stress is investigated to maximize output voltage without fracturing the crystal.

Section 2.3 discusses the electrostatic model that was used to compute electron beam ray-tracing from the emitters of the piezoelectric crystal. This analysis showed that divergence and sloped trajectory resulted in low electron beam intensity on the tungsten target. Charged particle optics were designed to correct for both phenomena and increase electron flux on the target.

2.2 Piezoelectric Modeling

Piezoelectric modeling began by drawing the crystal in a three-dimensional (3D) workspace. The Rosen piezoelectric crystal model consisted of two joined rectangular blocks of equal length, width, and thicknesses. These blocks represented the input and output ends of the piezoelectric transformer. Figure 2.1 shows the geometry for the Rosen transformer.

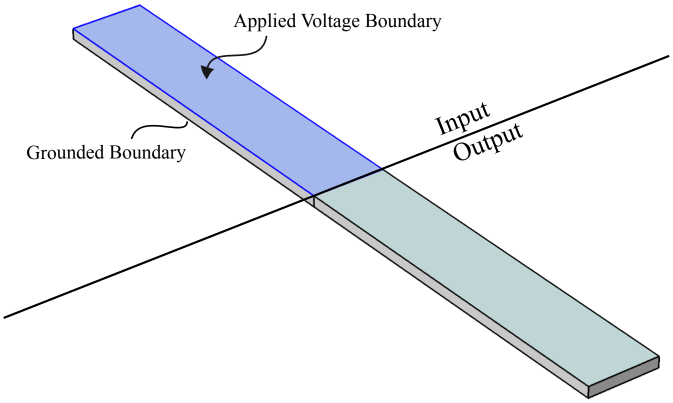

Figure 2.1: Three-dimensional drawing of piezoelectric crystal and electrical potential boundary conditions

Once the crystal was drawn, boundary conditions were applied to the surface of the input portion of the crystal to model the electrodes on the physical device. The blue highlighted region in Fig. 2.1 shows the applied voltage boundary with the grounded boundary on the obverse side.

Lithium niobate is included in the materials library of COMSOL and was selected to fill the 3D domains enclosed by the blocks. As discussed in section 1.2, the crystallographic rotation angle is an important parameter for the behavior of anisotropic piezoelectric materials, such as lithium niobate. The rotation angle is set with a rotated geometry function using Euler angles. An example of Euler rotation for the general case and the piezoelectric crystal model are shown in Fig. 2.2

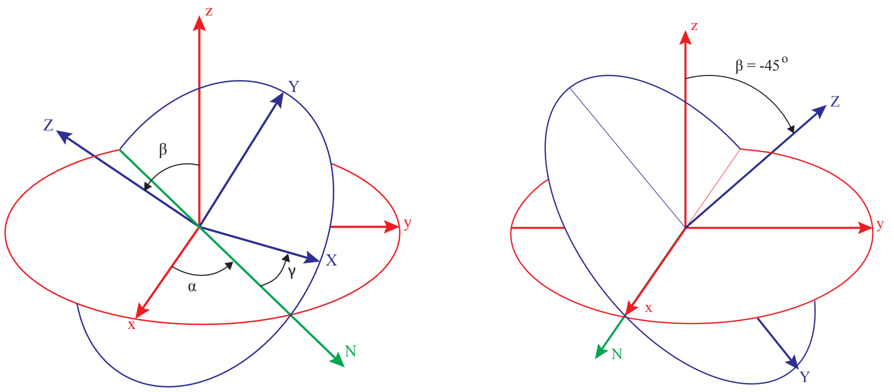

(a) General case (b) Z-rotated lithium niobate

Figure 2.2: Rotated coordinate systems using Euler Angles

Figure 2.2a shows the general case for a rotated coordinate system using Euler angles. Three parameters (α, β, and γ) are used to completely describe a rotated system. A reference system and a rotated system are equal when each parameter equals 0°. The first parameter, α, describes the angle between the reference x-axis (lower case x) and a reference axis called the line of nodes (N) about the z-axis. Next, β defines the angle between the reference z-axis and the rotated Z axis about the line of nodes. Lastly, γ defines the angle between the line of nodes and the rotated X-axis about the rotated Z-axis.

The orientation used in this model only requires the β parameter to define the crystallographic rotation of lithium niobate. As discussed in section 1.2, the transformer ratio of the crystal is maximized for the -45° rotated Z-axis. This is shown in Fig. 2.2b with $\alpha = 0°$, $\beta = -45°$, and $\gamma = 0°$.

Once the geometric, electrical, and material parameters were defined, an eigenfrequency solver was used to find the resonant frequency of the crystal. The eigenfrequency solver typically returned between $6-10$ frequencies, but only the frequency for length extensional mode is capable of producing high voltage. Figure 2.3 shows three examples of solutions for the eigenfrequency solver.

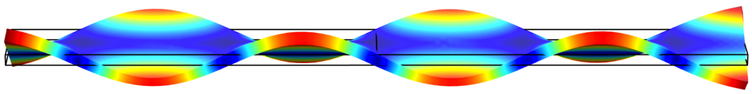

(a) f = 30501 Hz, Below the frequency for length-extensional resonance

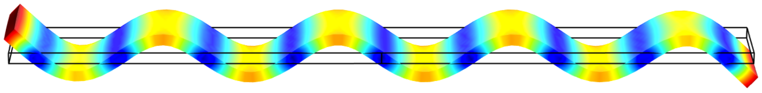

(b) f = 31733 Hz, Above the frequency for length-extensional resonance

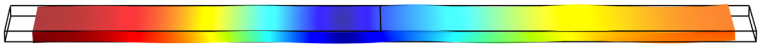

(c) f = 31214 Hz, Correct frequency for length-extensional resonance

Figure 2.3: Examples of eigenfrequency solutions showing various modes of resonance for the piezoelectric crystal model

Figures 2.3a and 2.3b show eigenfrequency solutions for modes other than the length extensional mode. A deformation plot shows resonant displacement in dimensions other than length, meaning that these frequencies are not the length-extensional mode. The color gradient corresponds to mechanical displacement with blue and red corresponding to low and high displacement, respectively. Figure 2.3c shows the length extensional resonance mode, characterized by displacement only along the length of the crystal. This mode is effective for voltage transformation and the associated frequency was used both in modeling and physical experiments.

Once the length-extensional resonant frequency was calculated, frequency domain analysis was used to determine output voltage and von Mises stress. Figure 2.4 shows a voltage gradient of a resonant piezoelectric transformer.

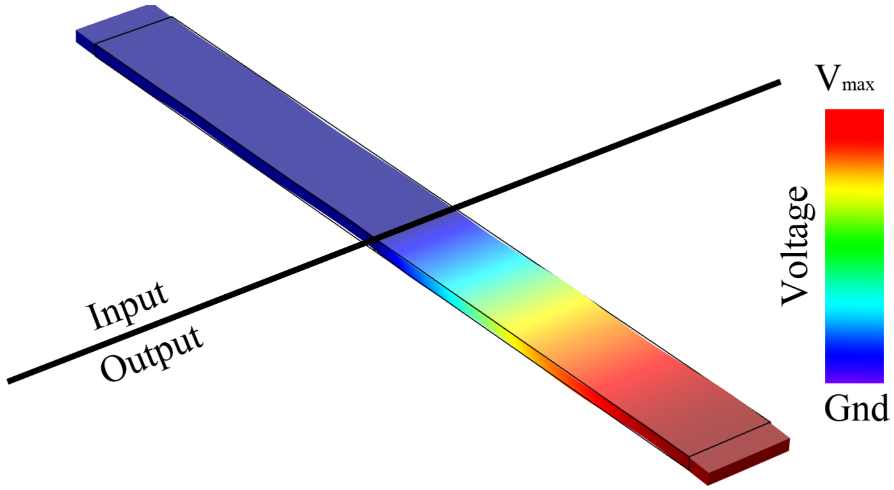

Figure 2.4: Voltage gradient and mechanical displacement for the length extensional resonant mode of a piezoelectric crystal

A line distinguishes the input and output ends of the crystal in Fig. 2.4. The input of the crystal is uniformly blue, corresponding to a low voltage magnitude applied across the entire input surface. On the output side, the voltage gradient along the length of the crystal is shown by a transition from blue to red, reaching a maximum voltage at the extremity of the bar. A deformation plot is used to show the mechanical displacement of the crystal. The displacement of the crystal is shown by comparing the color-filled shape to the black outline, which represent the energized and idle shapes of the crystal, respectively. The crystal was in an elongated state when the output voltage was negative. Not shown is the case of positive voltage, when the crystal was in a compressed state.

The voltage and electric field at the surface of the crystal were plotted as a function of position along the length of the crystal, shown in Fig. 2.5. The voltage at the input electrode voltage was uniform and approximately zero compared to the magnitude of the output voltage. The electrode terminated at the center of the crystal where the voltage magnitude began to increase non-linearly. The $d\mathrm{V}/d\mathrm{x}$ was largest near the electrode interface and smallest at the extremity. This is also shown in the electric field profile in Fig. 2.5. A peak in electric field occurred at the interface of the electrode and diminished towards the extremity of the output.

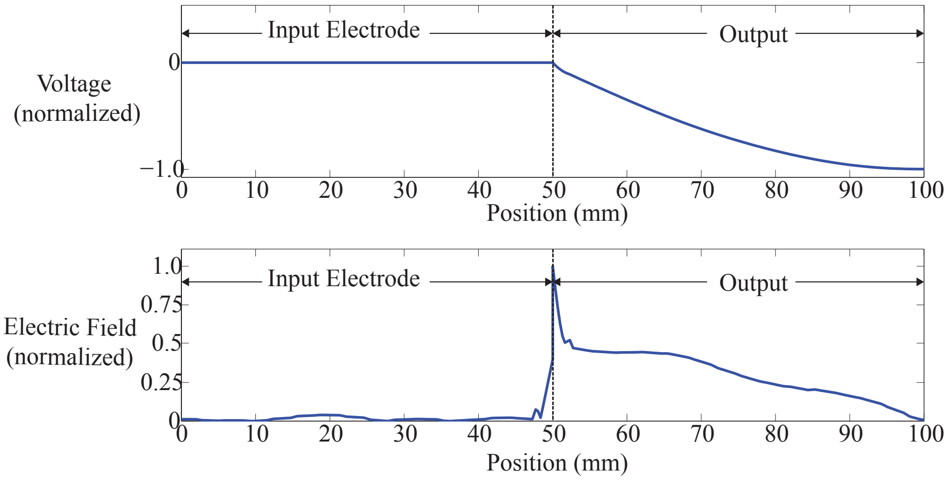

Figure 2.5: Electrical parameters of resonant piezoelectric crystal vs. position along length

The mechanical displacement and von Mises stress were plotted as a function of position along the crystal in Fig. 2.6. The displacement reached local maxima at each extremity, however, the displacement on the input side was higher than the output side. Additionally, the displacement minimum occured approximately 5 mm off-center towards the input, an effect that has been observed in previous studies [9]. The von Mises stress maximum was at the same position as the displacement minimum due to the longitudinal compression and expansion of the length-extensional resonant mode. This indicated that fractures are most likely to occur in the center of the crystal.

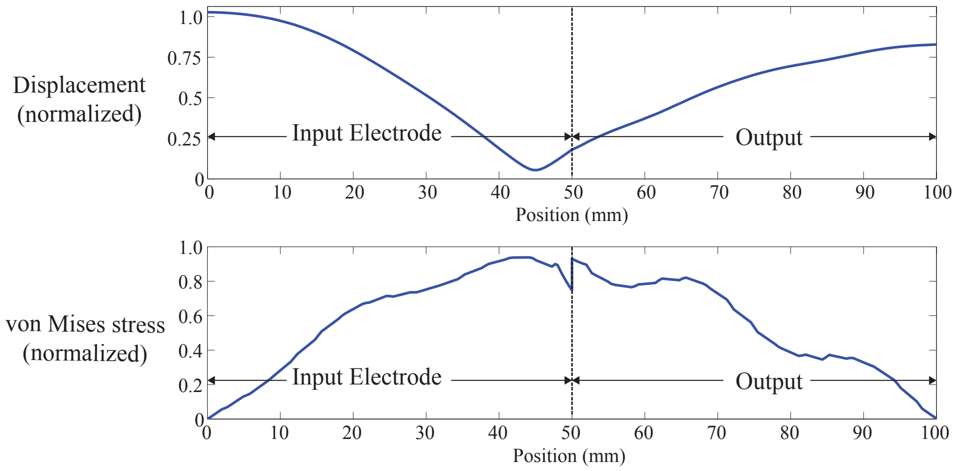

Figure 2.6: Mechanical parameters of resonant piezoelectric crystal vs. position along length

The output voltage and von Mises stress solutions were useful for determining an optimal input voltage that maximized output voltage while remaining below the yield strength of lithium niobate. Wong quotes the yield strength for lithium niobate to between 30−120 Mpa [41]. As input voltage increases, both output voltage and von Mises stress increase. This effect is shown in Table 2.1.

Table 2.1: Simulated output voltage and maximum von Mises stress for piezoelectric crystal operated at resonance for a range of input voltages. (∗ indicates experimental operating voltage)

Crystal Input Voltage (V)	Crystal Output Voltage (kV)	Maximum von Mises stress (Mpa)
1	11	4
6	68	29
11*	125	53
16	182	77

Table 2.1 shows that 6 V input produced a maximum stress of 29 Mpa, just below minimum quoted yield strength of 30 Mpa. This input voltage yielded an output of 68 kV, which is sufficient for x-ray applications, but falls short of the neutron source voltage of 100 kV. To reach the neutron source goal, the crystal must be operated at

higher input voltages, thus increasing the maximum stress on the crystal. An input voltage of 11 V increased the output voltage to 125 kV at the expense of increasing stress to 53 Mpa. Increasing the input voltage to 16 V further increased stress and output voltage. Since cross-sections for the D(d,n)^{3}He reaction at 125 kV and 182 kV are effectively equal, operating at 16 V provided little advantage and only increased the likelihood of fracturing the crystal due to excessive stress. For this reason, 11 V was chosen as the operating input voltage because it satisfied the neutron source voltage of 100 kV output with the least amount of stress on the crystal.

2.3 Electron Beam Optics Design

The electrostatic model was used to conduct ray tracing for an electron beam accelerated produced at the piezoelectric crystal output. This modeling was conducted to determine the approximate proportion of initial electron beam flux that was incident on the bremsstrahlung conversion target. A grounded cylinder was added to the model and placed 5 cm away from the crystal output. The ray-tracing simulation results are shown in Fig. 2.7.

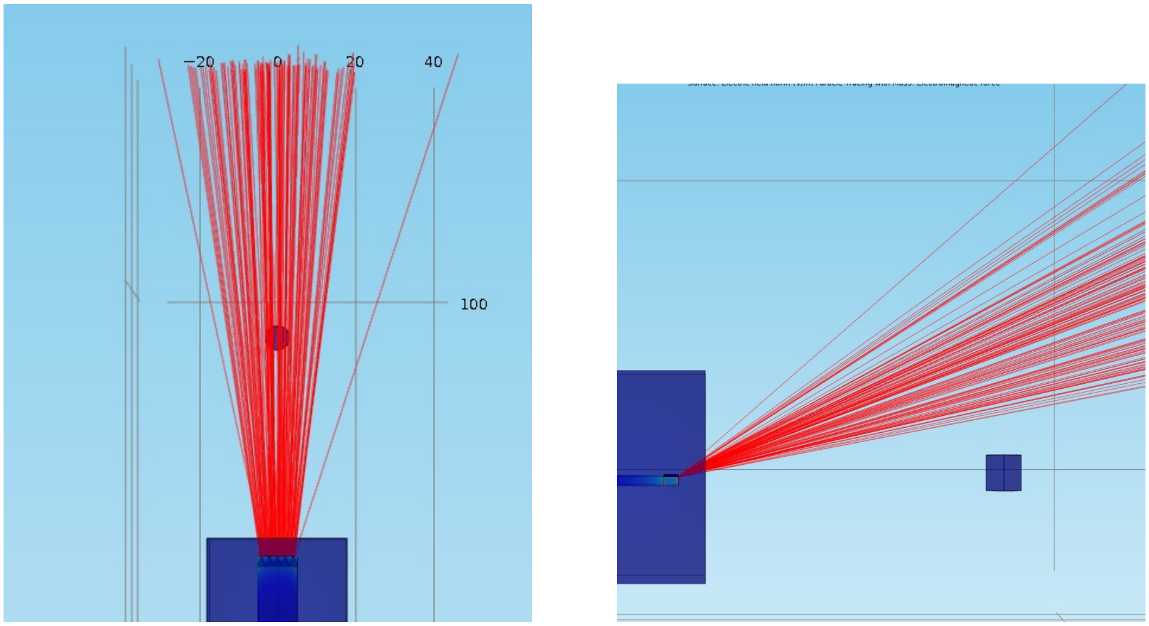

(a) Top view

(b) Side view

Figure 2.7: Electron beam ray-tracing without the use of optics

Figure 2.7 shows that two effects reduced the electron flux at the surface of the target. First, Fig. 2.7a is a top-down view of the electron beam showing that the beam diverged horizontally as it traveled away from the source. The side view in Fig. 2.7b shows the beam diverged vertically but also sloped upwards such that none of the electron flux was transmitted to the target. These results suggested that correcting for both the diverging effect and the sloping effect could substantially increase the electron beam flux at the target.

An investigation of the diverging beam effect was conducted first. The electrostatic model showed that the beam divergence was due to radial electric field lines from the output of the crystal. The electron beam tended to follow these lines, causing the beam to diverge. To solve this problem, a spherical ground plane was introduced to the model and placed 1 mm away from the output of the crystal. A diagram of the spherical ground plane is shown in Fig. 2.8.

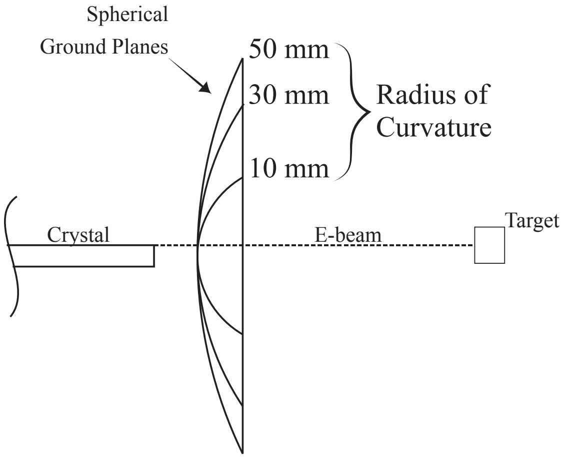

Figure 2.8: Spherical ground plane to correct for divergent beam. Three radii of curvature are shown.

The curvature of the ground plane was set to oppose the radially expanding electric field lines. A sweep of various radii of curvature was conducted to determine the optimal shape of the plane. A radius of 30 mm was experimentally determined to best reduce the beam divergence.

The sloping effect was determined to be caused by the position of the emitters on the crystal. A test was conducted where electrons were emitted directly from the center of thickness of the bar. In this case, the slope effect vanished. However, as the emission point moved toward the top surface of the bar, the slope became more prominent. In physical experiments, emitters are placed on the top of the crystal, offsetting the point of emission from center by 750 μm, or $1/2$ the crystal thickness. Due to the high electric fields near the surface of the crystal, this change resulted in the slope effect that was shown in Fig. 2.7b. To correct for this slope, angled metallic shielding was added to the model and placed 1 mm above the the crystal surface. A diagram of this surface is shown in Fig. 2.9.

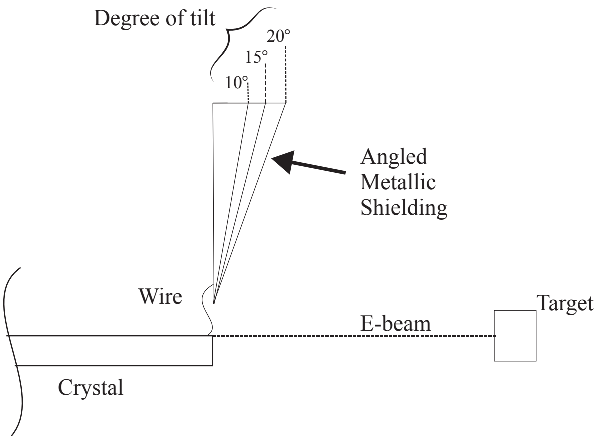

Figure 2.9: Angled metallic shielding to correct for the sloped electron beam. Three angles for the tilt of the shielding are shown

The potential of the shielding element was set to the same potential as the output of the crystal. The purpose of the shielding was to mimic the effects seen when the electrons were emitted from the center of the thickness. By placing a high voltage source above the crystal, it was predicted that the tilt of the beam would be reduced. Modeling showed that simply placing a flat plane near the output of the crystal was not enough to correct for the sloping of the beam, so the shielding was rotated at various angles. Rotating the shielding proved to effectively eliminate the sloping effect of the beam, and a rotation of 15° was determined to be the optimal angle for the shielding.

The spherical ground plane and angled shielding elements were coupled into a single device, and the results from the optics are shown in Fig. 2.10.

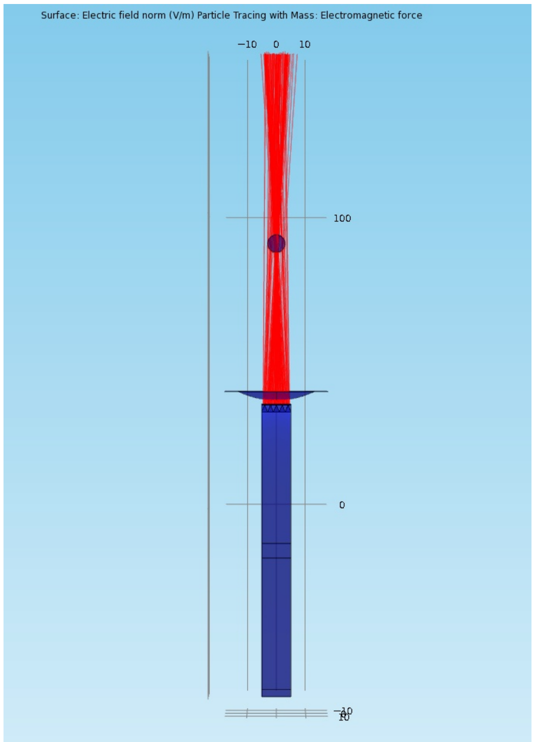

(a) Top view

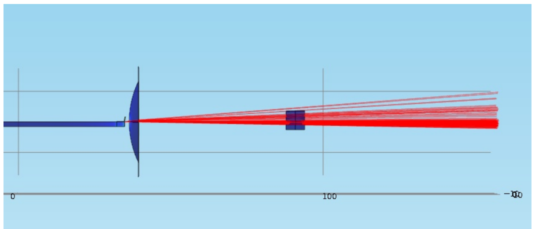

(b) Side view

Figure 2.10: Improved focusing provided by electron beam optics.

Figure. 2.10 shows that both the diverging and sloping effects of the beam were corrected with the electron beam optics. The top view in Fig. 2.10a shows that the horizontal divergence was eliminated and a focal spot was produced. The side view in Fig.2.10b shows that the slope was corrected by the angled shielding. Unlike the horizontal case, the vertical divergence was not completely eliminated; however, it was substantially reduced compared to the no-optics case.

The electron beam optics were designed in an electrostatic environment in which uniform planes of high voltage and perfectly transmissible grounded spheres were simple to deploy. In the physical device, the spherical ground plane was approximated by a metallic mesh surface which was deformed with a spherical mold with a 30 mm radius of curvature. The angled shielding support was made with acrylic and silver paint was applied to its surface. A wire was then adhered to both the output of the crystal and the angled shielding to couple the voltage between the two.

Electrostatic modeling of the electron beam showed that a large portion of the initial beam current was not interacting with the target. Using this model, electron beam optics were designed to increase the electron flux at the target. An increased electron flux was beneficial because produced higher count rates of bremsstrahlung x-ray radiation at the target, thus decreasing the time necessary to measure significant x-ray counts.

Chapter 3

Experimental Configuration

3.1 Overview

This chapter describes the experimental methods used to operate the piezoelectric crystal as a high voltage transformer and reliably monitor its performance. Crystal preparation methods are outlined and resonant mode operation is described. Equipment and system diagrams are presented and the diagnostics used to analyze crystal performance are described. Four experiments are presented which test the piezoelectric crystal as a high voltage source.

The first experiment is referred to as the initial experiment. The purpose of the initial experiment was to collect preliminary results regarding the viability of an x-ray voltage diagnostic. An electron beam diode extracted beam current from the piezoelectric crystal to produce x-rays on a small bremsstrahlung conversion target. An x-ray detector placed inside the vacuum test chamber was positioned directly next to the bremsstrahlung x-ray source to maximize geometric detection efficiency. The initial experiment established that the x-ray diagnostic was a practical technique for crystal voltage measurement and further work was conducted to optimize data collection methods and experimental configurations.

The second experiment in this chapter is the electron beam optics experiment. The objective of the experiment was to increase the x-ray flux produced by the piezoelectric crystal. Optics were used to focus the electron beam on the target. By focusing the beam, a higher proportion of the beam interacted with the target to produce x-rays. This increase in electron-to-x-ray conversion efficiency increased the total x-ray flux, resulting in improved counting statistics.

The third experiment in this chapter is the optimized configuration. The small x-ray target was removed from the experiment and the beam was accelerated directly into the grounded walls of the vacuum chamber. The chamber walls provided a large target for the electron beam to better produce x-rays. An x-ray window installed on the chamber wall provided improved x-ray detector positioning, resulting in increased measured count rates and measured maximum x-ray energy.

The final experiment in this chapter is the investigation of the piezoelectric crystal as a neutron source. Deuterium gas was flowed into the chamber as a deuterium ion source. Two methods were developed to produce and accelerate deuterium ions. The first method used field-ionizing tips as an ion beam diode on the surface of the crystal output. The second method used two independent piezoelectric crystals simultaneously to produce a deuterium rf plasma. The x-ray detector monitored crystal output voltage while an He-3 neutron detector monitored neutron production.

3.2 Device and Operation

3.2.1 Piezoelectric Crystal

The method for preparing a piezoelectric crystal for high voltage operation was standardized. The preparation included the application of input electrodes, wires, and field emitting tips to the crystal surface. The crystal was weighed throughout the preparation process to account for the accumulated mass. This provided a record

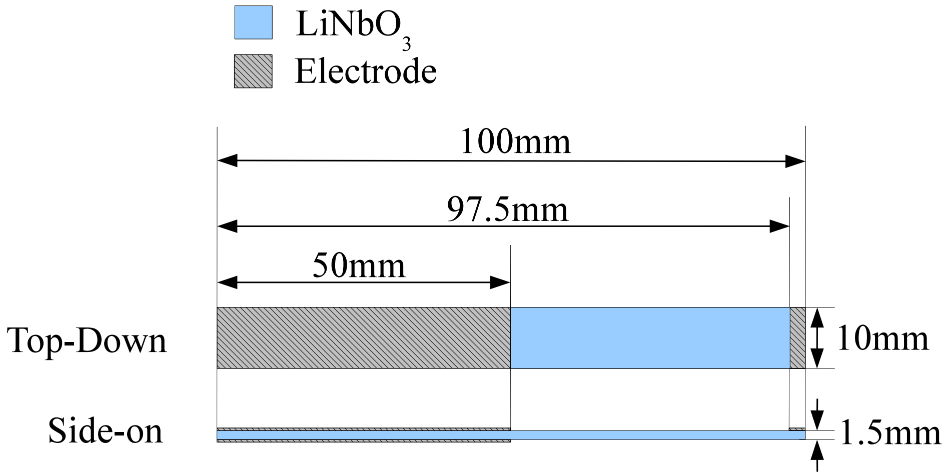

Figure 3.1: Electrode design for a high voltage piezoelectric crystal. Input electrodes on left of crystal, output electrode on right.

for each crystal as well as a treatment variable to test against device performance. A Kapton tape mask was applied to the surface of a bare crystal to begin the patterning process. Electrodes made from silver paint were painted on by hand using the mask to precisely and consistently define the electrode edges. After painting the electrode, the crystal was placed in an oven at a temperature between 60 ° and 80 ° C to expedite the paint curing. Figure 3.1 shows the final design of the patterned piezoelectric crystal.

Once the electrodes were cured, one 28 AWG single strand wire was attached to each of the input electrode surfaces using additional silver paint. The oven drying process was again used to reduce preparation time. Lastly, PtIr emitters were cut from wire stock using standard wire cutters to a length of $10 - 15$ mm and adhered to the output terminal of the crystal with silver paint. After curing the paint, the emitter tips were clipped at a 45 ° angle using a pair of Erem 612 N series diagonal cutters. These cutters are recommended for cutting SEM electron emitters because they produce sharp, microscopic tips [42]. Figure 3.2 is an image taken from Benwell [9] and shows the sharp tip profile of a mechanically cut PtIr tip.

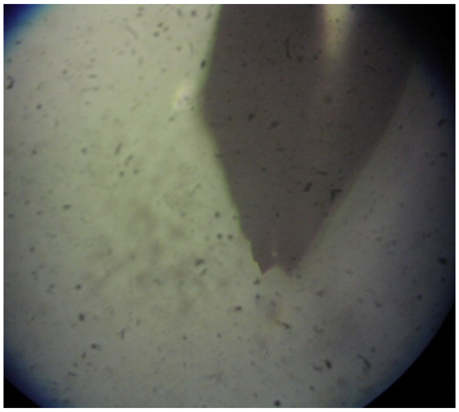

Figure 3.2: Sharp profile of a clipped PtIr wire emitter tip.

3.2.2 Equipment

An Agilent 33210A function generator was used to produce a frequency- and amplitude-controlled AC voltage. An Amplifier Research KAA1020 power amplifier increased the AC voltage from $70\,\mathrm{mV}_{pp}$ to $32\,\mathrm{V}_{pp}$. A Pearson 2877 current transformer with $1\,\mathrm{V/A}$ output sensitivity measured the input current to the crystal. A Tektronics TDS 2024B oscilloscope measured crystal input voltage and current. An Amptek PX4 digital pulse processor interfaced a PC running MCA software to an Amptek x-ray detector. A Stanford Research Systems DG535 digital pulse generator gated the PX4 such that the live-time of the detector coincided with applied bursts to the crystal. A system diagram of the basic experimental configuration is shown in Fig. 3.3.

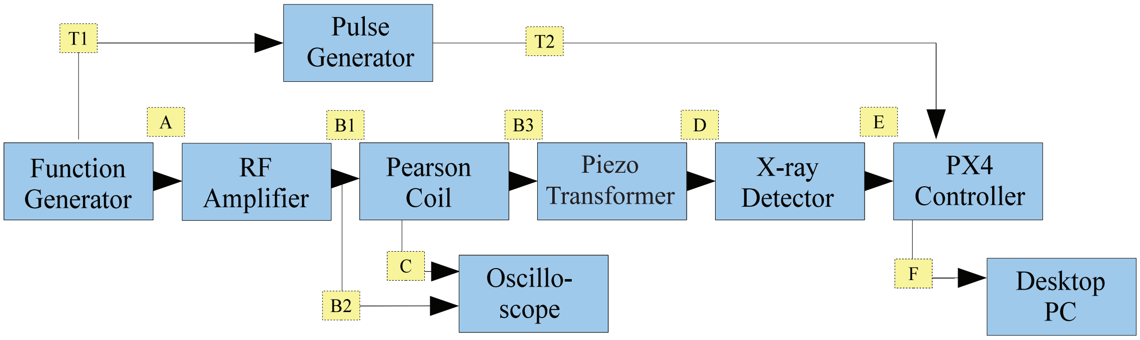

Figure 3.3: System diagram for the basic experimental configuration for piezoelectric crystal operation. (A): Low voltage AC drive signal 50 mVpp- 100 mVpp 30.7 kHz;(T1, T2): Falling edge trigger, Gate signal for PX4; (B1, B2, B3): High voltage AC drive signal 20 Vpp- 40 Vpp to Pearson coil, Oscilloscope, and Crystal; (D): Crystal-generated x-ray flux; (E): Raw analog x-ray detector signal; (F): Digital spectrum data;

Two expanded polymer sponges support the crystal while keeping mechanical damping to a minimum. The sponges lightly clamp the crystal and suspend it above the circuit board. The crystal is positioned between the sponges so that clamping pressure is distributed evenly over the crystal center, the point with the least amount of displacement. The crystal is therefore supported with minimal mechanical drag. Figure 3.4 is a photograph of a crystal resting within the sponge clamp.

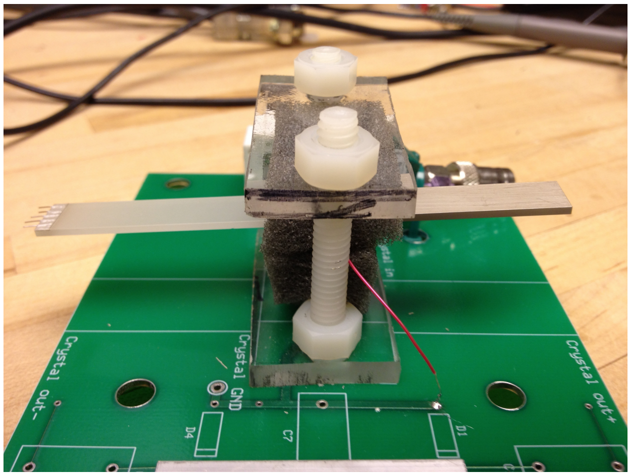

Figure 3.4: Piezoelectric transformer resting in a sponge clamp on a circuit board.

3.2.3 Resonant Operation

Operation of the piezoelectric crystal is highly dependent on frequency. This requires the input AC frequency to match one of the crystal's mechanical Eigen frequencies. These frequencies are predominantly determined by the geometry of the piezoelectric crystal [43]. A one-dimensional model based on Yang [18] was created that used the equations of elastic motion, piezoelectric effects, and the material constants for lithium niobate. Figure 3.5 shows the frequency dependence of gain as calculated by this model.

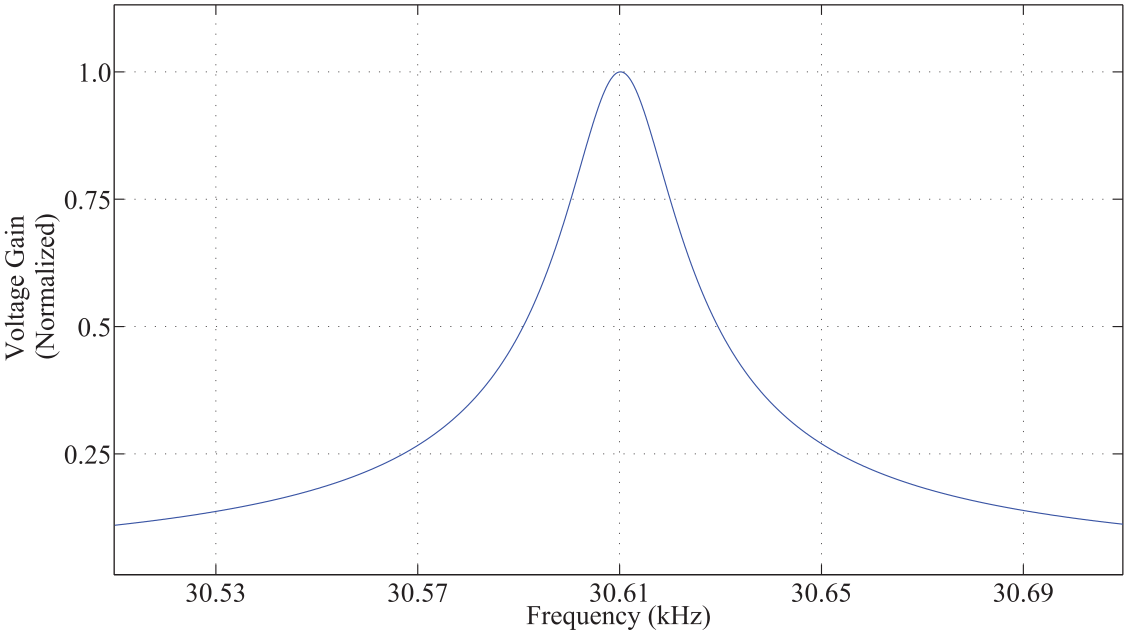

Figure 3.5: Frequency response of the gain for a 100 mm piezoelectric crystal.

The piezoelectric crystal is a high Q device, a fact that is exploited to produce voltage gains on the order of 6000. However, the drawback of such a high Q is that there is a very narrow band of operational frequencies as shown in Fig. 3.5. There must be a high degree of frequency control to ensure the crystal runs with the full voltage gain.

Equation 3.1 is used to estimate the resonant frequency, ω_n. This calculation uses material properties of lithium niobate and the dimensions of the crystal [9]. The variables l, s^E, and ρ are the length of the bar in the x_2 direction, the elasticity tensor, and the density of the material. The integer value n indicates the harmonic mode of resonance.

$$\omega_n = \frac{n\pi}{l}\sqrt{\frac{s^E}{\rho}} \tag{3.1}$$

Each crystal has a unique resonant frequency due to uncontrolled parameters such as electrode layer thickness and manufacturing tolerances. The procedure to find resonance is to sweep input voltage frequencies near the Eigen frequency of the crystal until the input current is in phase with the input voltage. Figure 3.6 shows how the phase relationship between voltage and current changes as the applied frequency approaches, reaches, and then passes the natural resonance of the crystal. Once resonance of the crystal has been determined, the frequency is recorded and the sample is ready to enter the vacuum chamber for testing.

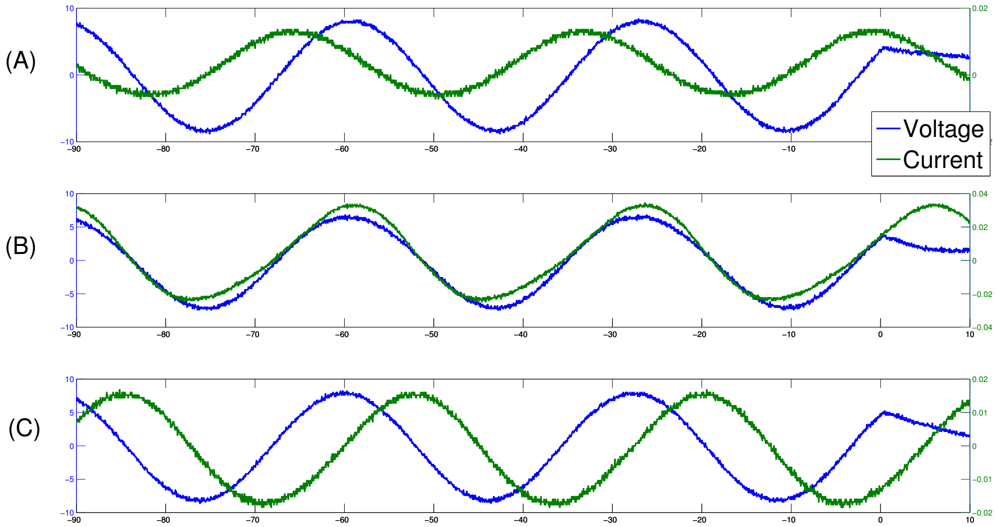

Figure 3.6: Example of the input voltage and current phase relationships for A) 10 Hz below resonance, B) On resonance, and C) 10 Hz above resonance.

Piezoelectric crystals have demonstrated a high likelihood to fracture when driven with excessive input voltage amplitude. Figure 3.7 shows a collection of piezoelectric crystals that have fractured throughout the experimentation. This fracturing is often attributed to exceeding the von Mises yield strength of lithium niobate. In practice, it has been found that an input voltage of 32 V_{pp} is within the safe operational range for the crystal and anything above 45 V_{pp} is in severe risk of fracture.

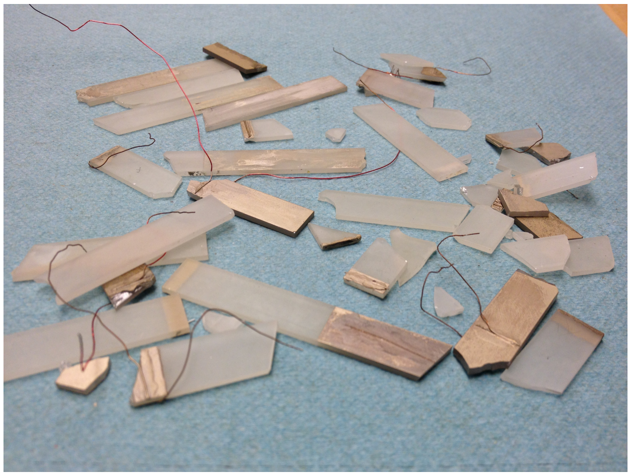

Figure 3.7: Fractured piezoelectric crystals as a result of exceeding the von Mises yield strength of lithium niobate.

3.3 Diagnostics

Two x-ray detectors were used in this experiment: the Amptek XR-100CR Si-PiN detector and the Amptek XR-100T CdTe γ/x-ray detector. The Si-PiN detector is used for detecting x-rays with a maximum energy of 30 keV. Above this energy, the detection efficiency drops quickly (Fig A.6a). The CdTe detector is capable of measuring x-ray energies over 100 keV (Fig A.6j) [44]. A limitation of the CdTe detector is that it is highly sensitive to mechanical and acoustic interference. Shaking, vibrating, or otherwise perturbing the CdTe detector while in operation fills the MCA spectrum with false counts. This made it impractical to place the detector inside the vacuum chamber because the vibrations of the pump system coupled into the detector. Shutting off the pump system did not solve the problem because vibrations from the crystal interfered with the detector. Vibrations from the crystal traveled through the wires on the input electrodes, into the circuit board, and into the walls of the chamber to reach the detector. As a result, the CdTe detector could only be operated outside of the chamber.

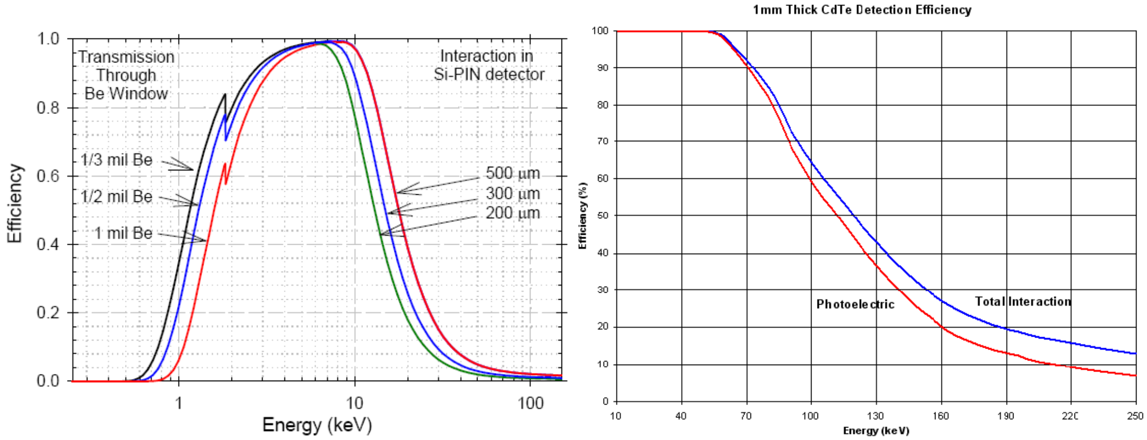

(a) XR-100CR SiPiN (b) XR-100T CdTe

Figure 3.8: Amptek X-ray Detection Efficiencies.

The MCA was calibrated using a Spectrum Techniques 1 μCi Cd-109 calibration source for the CdTe x-ray detector. The Amptek manual suggests that the two calibration peaks should be chosen such that one peak lies within the low energy region of the spectrum and the other peak at the high energy region. Cd-109 is a convenient choice because it has prominent peaks at 22 keV and 88 keV. Table 3.1 shows select decay properties of Cd-109. Figure 3.9 shows a sample calibration spectrum of the Cd-109 source.

Table 3.1: Pertinent decay properies of Cd-109 as an x-ray detector calibration source.

E (keV)	I (%)	Channel
21.990	29.5	171
22.163	55.7	173
24.912	4.76	194
24.943	9.2	195
88.043	3.61	673

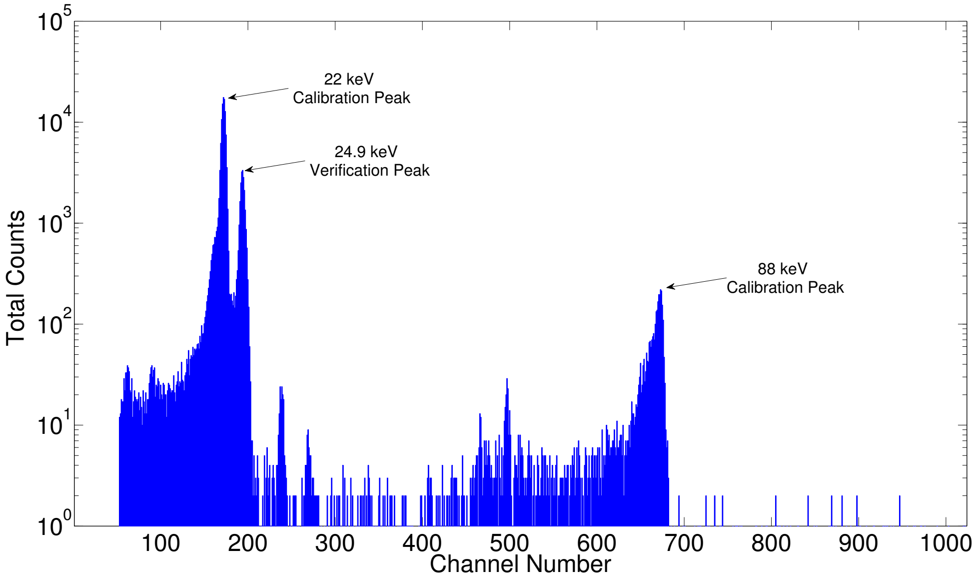

Figure 3.9: Sample calibration spectrum using the CdTe x-ray detector for a Cd-109 radioisotope calibration source.

The MCA was calibrated using the peak centroids located at channels 172 and 673. As shown in table 3.1, there are actually two distinct peaks very near to one another in energy at approximately 22 keV. These two peaks were too close to be resolved, so they were combined and their energies were approximated to 22 keV to form the first calibration peak. The second calibration peak was the 88 keV peak which occurs at channel 673. The peak at 24.9 keV is again the result of two distinct peaks and was used as a verification peak. Indeed, after calibration was completed, the MCA assigned this peak a value of 24.5 keV, independently verifying the calibration of the detector within reasonable error. The detector has a maximum energy range of 135.20 keV with these settings.

Background counts were collected for each x-ray spectrum. A large number of background counts were collected to reduce relative error of the measurement [29]. Background spectra were normalized to the runtime of the experiment and directly subtracted out of the sampled spectrum. The propagation of error, σ_f, was calculated as described by equation 3.2 where σ_{bg} and σ_{esp} refer to the square root of counts for the background spectrum and experimental spectrum, respectively.

$$\sigma_f = \sqrt{\sigma_{bg}^2 + \sigma_{exp}^2} \tag{3.2}$$

The piezoelectric crystal was operated in a pulsed mode with 3000 cycles per pulse and a duty cycle of 10%. In an effort to reduce the effect of accumulating background counts on the MCA spectrum, a digital pulse generator was used to gate the detector. The gated detector only recorded counts during the gate pulse, increasing the signal-to-noise ratio of the recorded spectrum. A Tektronics TDS 2024B oscilloscope was used to collect input voltage, input current, and the gating pulse. An example of this output is shown in Fig. 3.10.

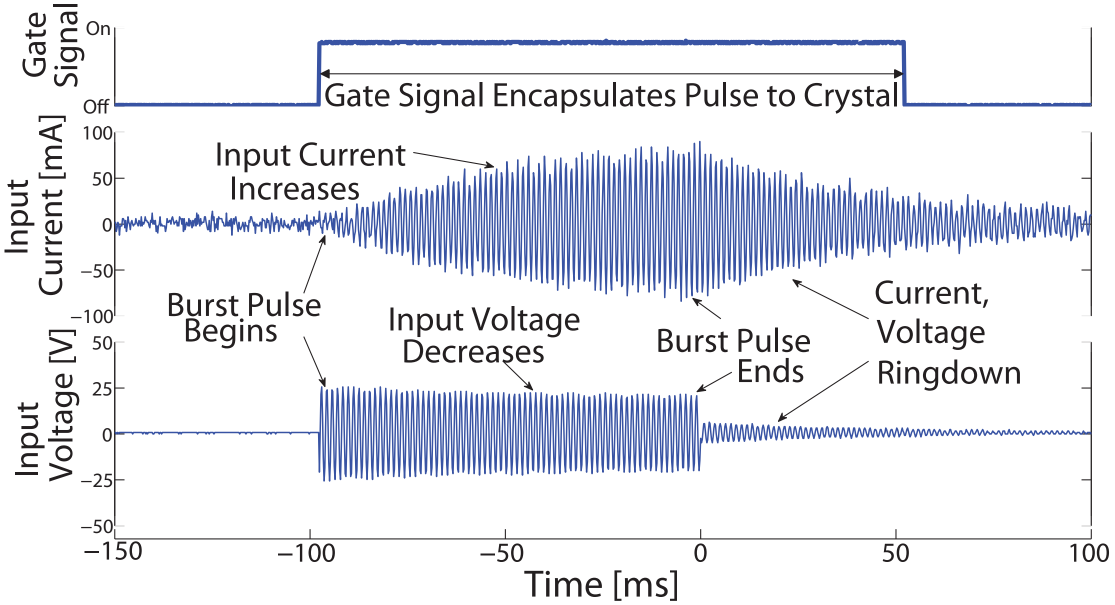

Figure 3.10: Gate, input current, and input voltage for a single burst.

The gate signal pulse is shown in Fig. 3.10 as an encapsulation of the applied burst pulse and the subsequent ring-down. This portion of the ring-down was arbitrarily defined as the 5 ms after the pulse and was included to count x-rays measured during this time. This figure also shows the characteristic burst behavior for input current and voltage to the crystal. At the beginning of the applied pulse, the voltage is at a maximum and the current at a minimum. As the burst continues, current increases while voltage decreases, corresponding to a drop in input impedance. This effect is a second method to confirm resonance in addition to the current and voltage phase alignment described in section 3.2.3 [9].

A binning technique was implemented for the x-ray spectra to increase the number of counts and improve endpoint determination. The 1,024 discrete channels of the MCA were consolidated to between ten and fifteen bins. As a result, the number of counts in those bins increased, resulting in a smaller relative error. Binning improved the statistics of the x-ray spectra, particularly at the highest energies where counts were much fewer in number. A drawback of this process is the reduced energy resolution of the spectrum. This proved to be of little concern because detailed spectral information pertaining to specific x-ray energies was not of particular interest for this experiment.

3.4 Methods

3.4.1 Initial Experiment Configuration

The initial experimental configuration for the piezoelectric crystal as a high voltage source included a crystal, a tungsten target, and an x-ray detector. Figure 3.11 shows a diagram of the initial configuration. The target was a one cm long by 1 cm diameter cylinder positioned approximately $5 - 10$ cm away from the crystal output. Electron emitting tips were attached to the other opposite output and directed towards the target. The electron beam was accelerated towards the target, producing bremsstrahlung radiation which was sampled by the x-ray detector.

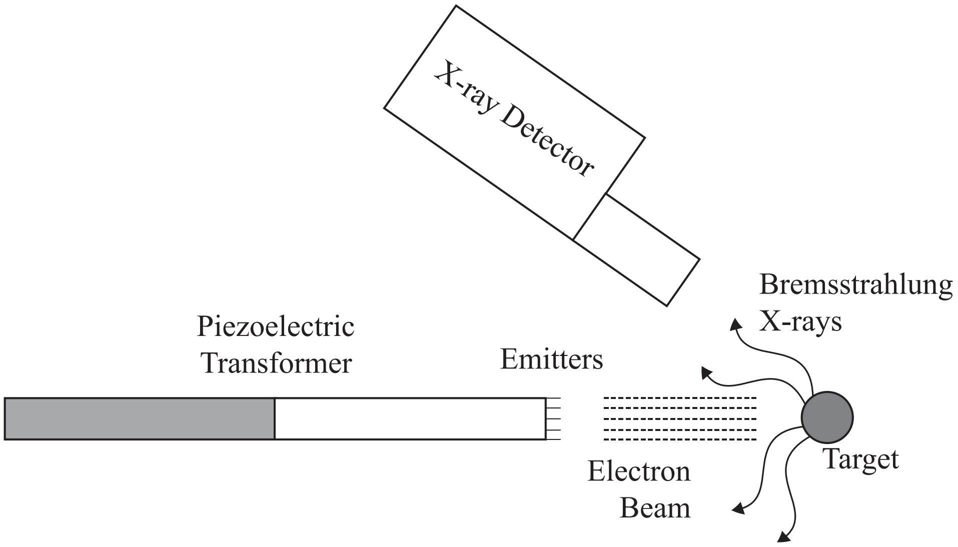

Figure 3.11: Initial configuration for producing x-rays with the Rosen piezoelectric crystal geometry.

3.4.2 Electron Beam Optics

Electron beam optics were developed in order to increase the electron beam intensity on target. As discussed in section 2.3, two beam-focusing elements made up the electron beam optics. A spherical mesh screen focused the beam while an angled metallic surface leveled the angle of departure. Figures 3.12a−3.12c show the electron beam optics.

Figure 3.12a shows the front view of the electron optics mount. The direction of beam travel is out of the page. The front view shows the spherical grid with a triangular piece of acrylic behind it. The angled metallic surface is silver paint patterned over this acrylic. A side on view of the optics is shown in Fig. 3.12b. Here, a notch in the aluminum chuck allows for the triangular acrylic to rest inside the optics. Figure. 3.12c shows the interchangeable set of different mesh sizes. Mesh size

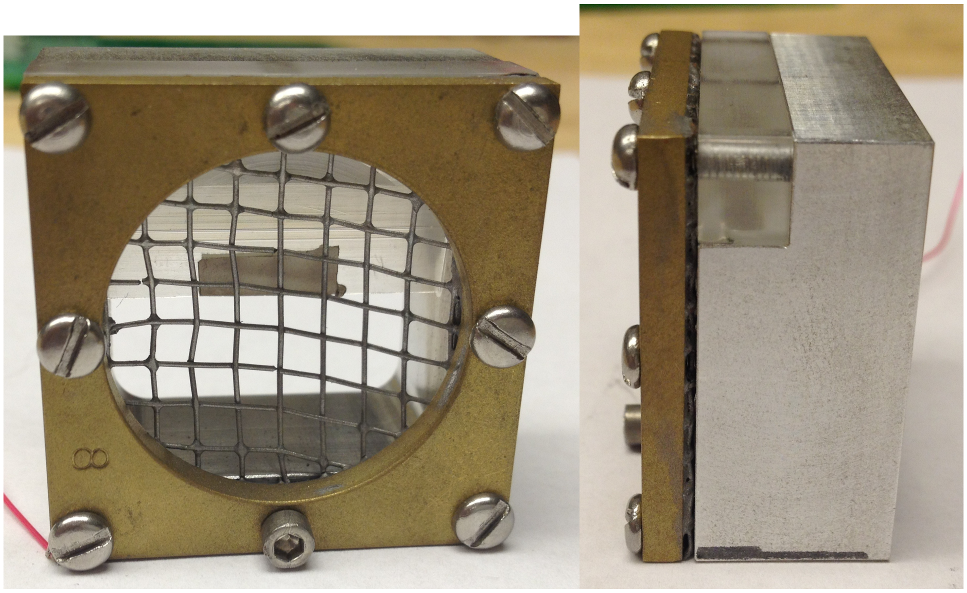

(a) Front view of optics (b) Side view of optics

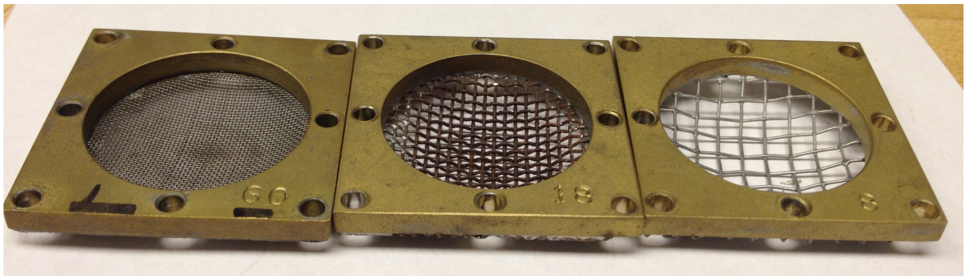

(c) Assortment of interchangeable mesh sizes

Figure 3.12: Photographs of electron beam optics.

is the number of openings within a linear inch of the wire mesh. For example, 3×3 mesh size means there are three openings horizontally and three openings vertically in one square inch. The three different mesh sizes were 60×60 (30.5 % open area fraction), 18×18 (41.1 % open area fraction), and 8×8 (60.2 % open area fraction).

An experiment was developed to determine if optics were effective in focusing the electron beam. This experiment used a target placement mount with variable horizontal positioning. Five positions were swept and the resultant x-ray energy was recorded for each position. The optics were considered effective if there was a significant difference in both x-ray energy and count rate among these positions. In particular, the center position should produce the highest energies and count rates as a result of the beam focusing.

3.4.3 Optimized Experiment Configuration

The final iteration of the piezoelectric x-ray diagnostic was an optimized version of the initial configuration. Two primary limitations associated with the basic configuration were eliminated. The primary disadvantage of the basic configuration was that the CdTe detector could not be used. The initial configuration required the x-ray detector to be positioned in the vacuum chamber next to the target. However, as discussed in section 3.3, the CdTe detector cannot be used inside the vacuum chamber. This meant that any experiment conducted using the basic configuration must use the Si-PiN detector, which limited the maximum detection energy to approximately 30 keV. The optimized approach used the stainless steel walls of the vacuum chamber as a target. This provided a target with much more surface area as compared to the tungsten target, increasing the likelihood of x-ray production. A diagram of the optimized configuration is shown in Fig. 3.13

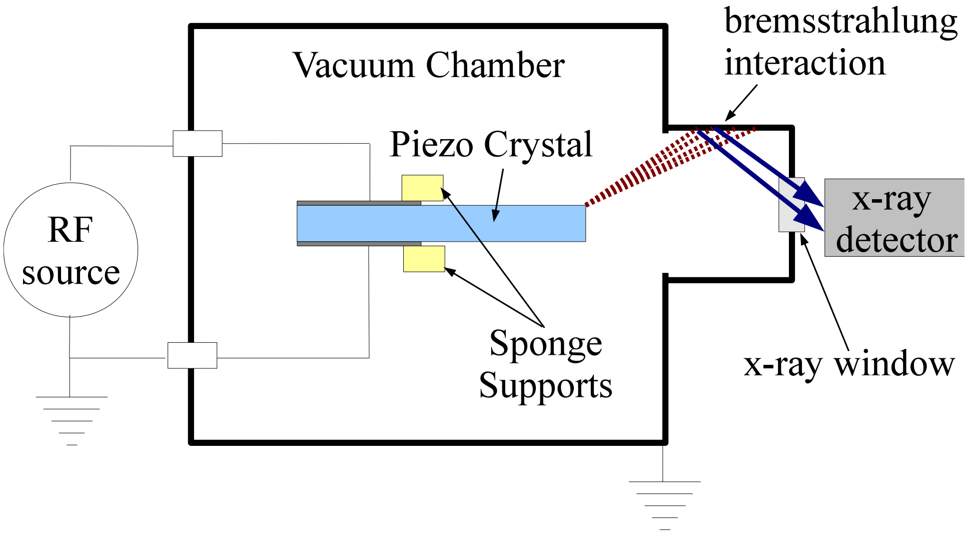

Figure 3.13: Experimental configuration for the optimized appoach for producing x-rays.

The piezoelectric crystal is positioned such that the emitters are facing down a port of the chamber. At the end of this port is a 50 μm thick Al window which allows for the transmission of x-rays. The CdTe detector is then placed on a camera tripod and positioned such that its viewport is next to this window. This places the detector close to the x-ray source, increasing the likelihood of x-ray detection.

The optimized configuration was robust enough to support a parametric sweep of operating conditions to learn more about the piezoelectric crystal and improve its performance. Several parameters were varied to construct a characterization of the crystal. Among these parameters were the number of emitters present on the crystal output, the base pressure of the chamber, the drive voltage to the crystal, and the duty cycle for the crystal. In addition to these parameters, multiple crystal samples were used and metrology was conducted to record electrode, wire, and emitter mass. These parameters were compared against x-ray count rate and maximum x-ray energy. Time-resolved x-ray data was collected during these experiments by recording multiple spectra throughout the duration of a test. A spectrum was manually recorded every 1−5 seconds of live time. This allows for detailed information about the time-dependent behavior of x-ray production from the piezoelectric crystal.

3.4.4 Plasma Generator

The plasma generator configuration was based on a dual Rosen geometry. In this experiment, two lithium niobate piezoelectric crystals were operated in parallel. Since each crystal has a different resonant frequency, two independent drive lines were required to operate the plasma generator. The primary line was tuned to the resonant frequency of one of the crystals and the secondary line was tuned to the other. The secondary line was set to trigger off the leading edge of the primary line, ensuring that both crystals were energized simultaneously. A system diagram of the piezoelectric plasma generator can be seen in Fig. 3.14.

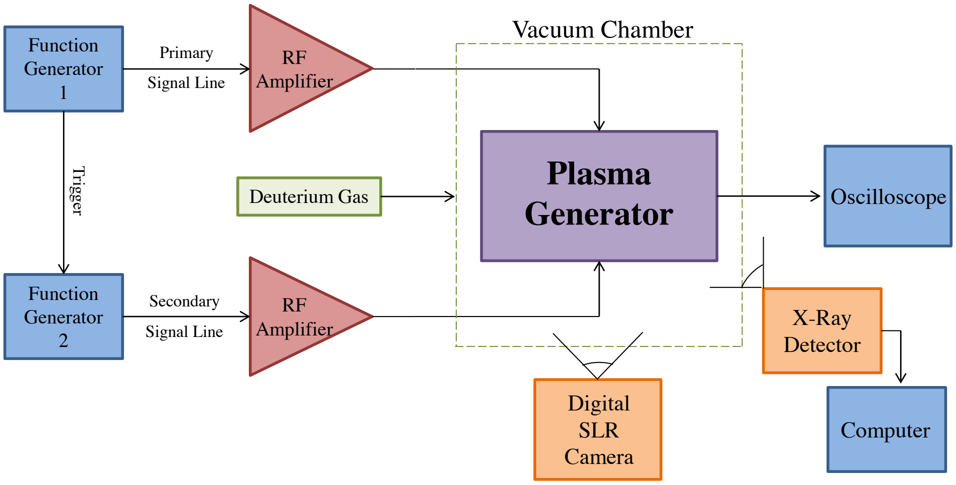

Figure 3.14: Plasma generator System Diagram.

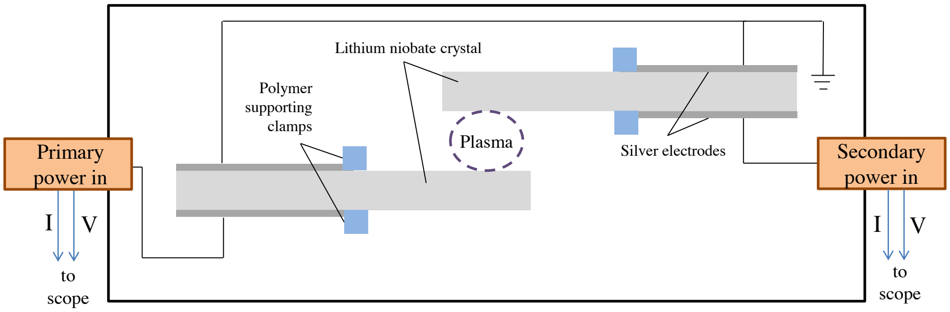

Figure 3.15: Plasma generator experimental configuration.

To produce a plasma, the piezoelectric crystals were arranged in a partially overlapping fashion. A one cm gap separated the two high voltage output terminals of each crystal. This formed a region of high electric fields where an rf plasma formed. A diagram of this configuration can be seen in Fig. 3.15. Two current transformers were used to measure the input current to each of the crystals. The deuterium pressure was regulated to a range of $9 - 25\,\mathrm{mTorr}$ by throttling a gate valve to a turbo molecular pump. A Sony α350 dSLR digital camera was used to image the plasma. The camera settings were fixed such that each image could be directly compared to one another. These settings are shown in table 3.2

Table 3.2: Settings for Sony α350 dSLR digital camera

EV	+0.0
ISO	1600
Focal Length	70 mm
F Stop	f/5.6
Shutter	30 sec

The amount of plasma produced at each pressure was not absolutely measured, rather the plasma luminosity was recorded by the digital camera and was used to infer the amount of plasma at each pressure on a relative scale. The CdTe x-ray detector was used throughout the experiment to monitor generator output voltage.

Chapter 4

Results

4.1 Overview

This chapter contains results acquired from experiments discussed in chapter 3. The first section describes how the initial configuration was used to validate the x-ray voltage diagnostic concept. X-ray counts were integrated over long periods of time and it was shown that the crystal was capable of producing x-ray energies of up to 30 keV. Electron beam optics were used to decrease the time necessary to measure high energy counts by increasing the electron flux on the target.

Results from an optimized configuration show that x-rays with energies greater than 100 keV were produced with the piezoelectric crystal. The production of x-ray count rates was observed to be time dependent and a theoretical analysis is conducted to explain the effect. A series of experiments were designed to test this analysis using a parametric investigation of five variables. The results from the parametric investigation show that the number of emitters on the crystal has an effect on the time dependence of x-ray production.

Lastly the plasma generator results are presented and discussed. The generator was operated over a range of pressures and the plasma was imaged throughout this range. The amount of plasma in the generator increased with pressure until 25 mTorr when the crystal could no longer sustain resonance. X-ray measurements were made throughout the experiment and showed that the generator reached 125 keV at 9 mTorr, but dropped below 8 keV as the pressure increased.

4.2 Initial Experiment and Electron Beam Optics

This section discusses the earliest data obtained from the piezoelectric crystal operated as an x-ray source. The initial experiment showed that the Rosen electrode geometry for the crystal was a viable method to produce x-rays. These early experiments established the basic experimental and data analysis techniques which led to the optimized configuration. Long periods of operation were required to measure significant counts, so electron beam optics were used to increase electron flux.

4.2.1 Initial Experiment Results

The initial experiment was conducted using the Rosen crystal geometry with a drive voltage of 11 V amplitude at a pressure of 5.00×10^{-6} Torr. A diagram for the initial experiment is shown in Fig. 4.1, and a respective x-ray spectrum is shown in Fig. 4.4. Scribed and cut platinum-iridium (PtIr) field emitters were attached to the crystal output electrode to provide high field enhancement for electron emission. A small tungsten cylinder was used as an electron beam target to produce bremsstrahlung radiation. The Si-PiN x-ray detector was placed in the vacuum chamber and directed towards the tungsten target. X-ray spectra generated from this configuration are shown in Fig. 4.2.

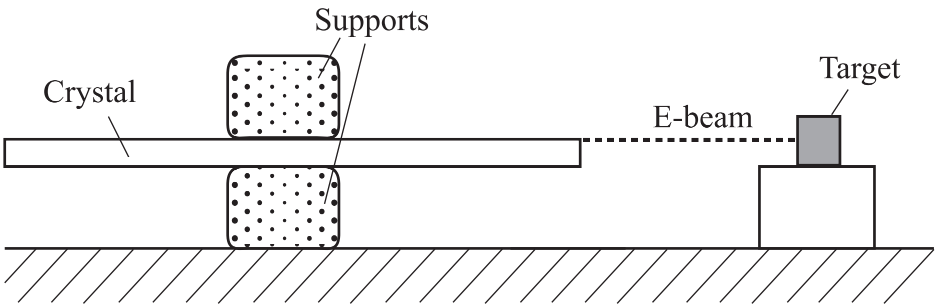

Figure 4.1: Diagram of crystal, and target for the intial experiment.

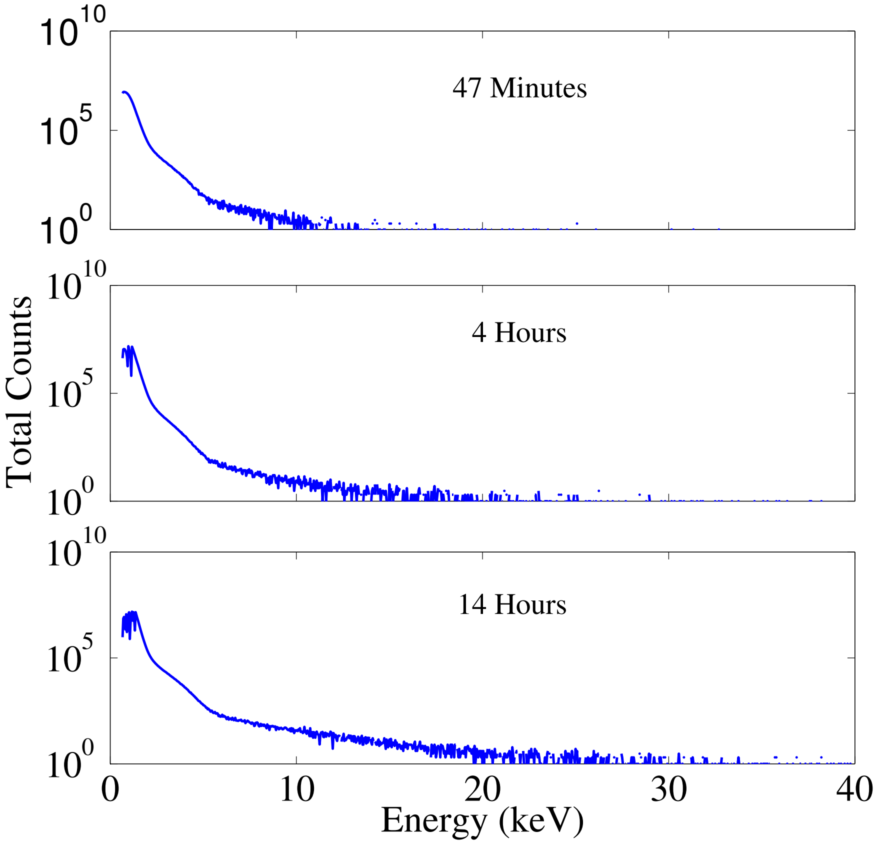

Figure 4.2: X-ray spectra generated using the initial configuration for three of sampling times during a single run.

The spectra in Fig. 4.2 were produced during one continuous period of operation at intervals of 47 minutes, 4 hours, and 14 hours, respectively. The x-ray spectrum reached an endpoint energy of approximately 10 keV in the first 47 minutes of operation. As the crystal continued to operate, more high energy counts were measured. The maximum endpoint energy after 4 hours was 20 keV, and after 14 hours was 30 keV.

4.2.2 Electron Beam Optics Results

Electron beam optics were used to increase the electron flux at the target, thus increasing the probability of measuring x-rays and decreasing the time required to record high energy counts. A diagram for the optics experiment is shown in Fig. 4.3, and a respective x-ray spectrum is shown in Fig. 4.4. Optics were mounted on the circuit board with the crystal and consisted of the spherical mesh to focus the beam and an angled metallic surface to correct for beam tilt as described in section 3.4.2. The output terminal of the crystal was inserted into the optics with the emitters approximately 1 mm away from the focusing grid. A wire was attached with silver paint to connect the crystal output to the angled metallic surface.The tungsten target was placed 10 cm away from the optics and the Si-PiN x-ray detector was used in the same arrangement as the initial configuration.

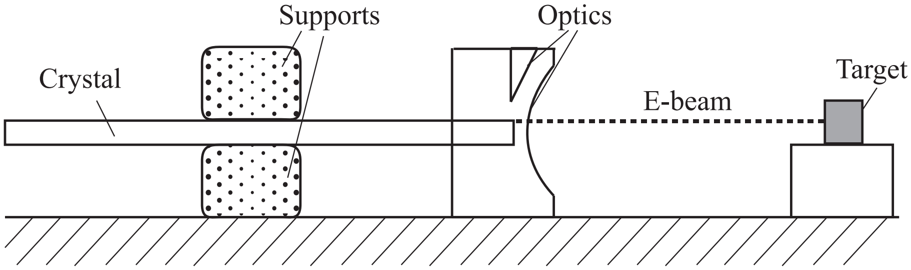

Figure 4.3: Diagram of crystal, optics, and target for the electron beam optics experiment.

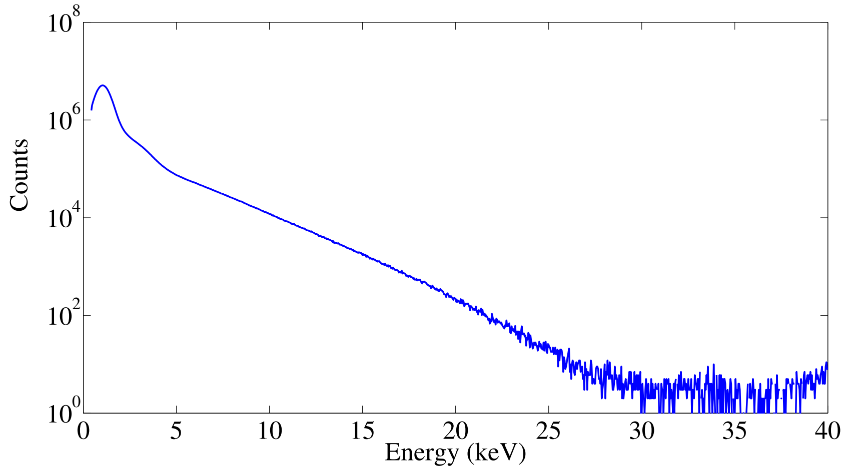

Figure 4.4: X-ray spectrum produced using electron beam optics showing increased counts and endpoint energy compared to the initial configuration.

The spectrum shown in Fig. 4.4 was integrated over 3.6 hours and background corrected. The optics improved the counts by a factor of 10^3 at 10 keV and by a factor of 50 at 20 keV compared to the 4 hour initial configuration case. An endpoint energy of 30 keV was measured when the optics were used and 20 keV was measured in the initial experiment. Overall, this increase in both counts and endpoint energy demonstrated an improvement over the initial case.

The beam profile and focusing was tested by moving the target into and out of the predicted focal point of the beam as determined by Comsol modeling from section 2.3. Increments of 1 mm were used to define five positions for the target and are referred to as -2 mm, -1 mm, 0 mm, +1 mm, and +2 mm. The results of this experiment are shown in Fig. 4.5.

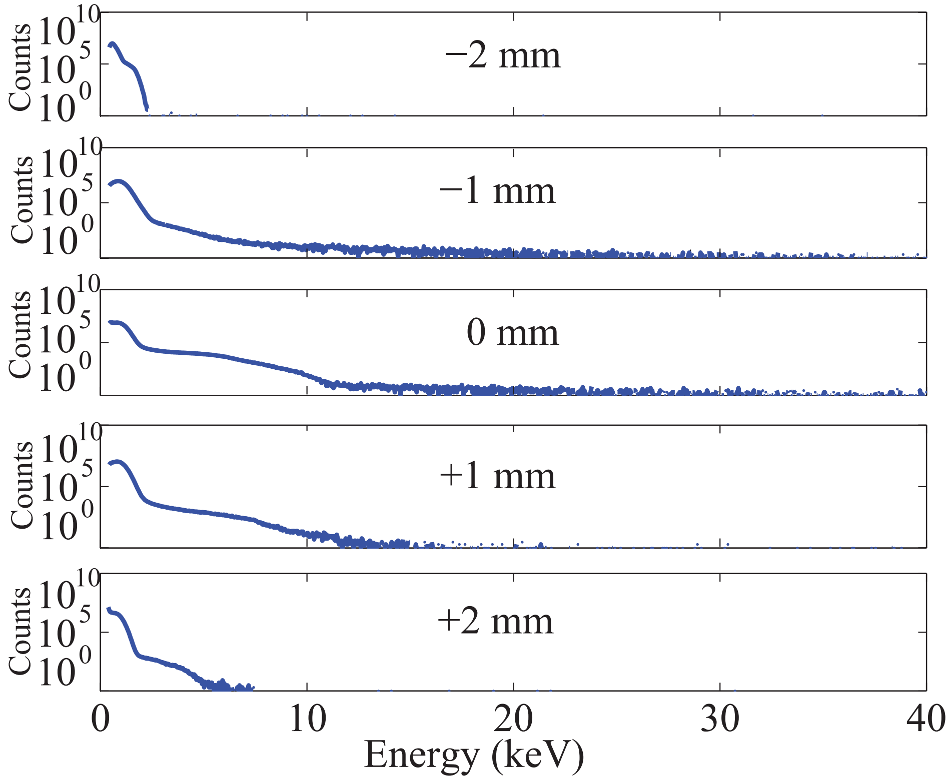

Figure 4.5: Results of the focus test for the electron beam optics. Positions references correspond to horizontal displacement of target from beam focus of -2 mm, -1 mm, 0 mm, 1 mm, and 2 mm.

Figure 4.5 shows that the most counts and highest endpoint energy were measured when the target was placed in the center of focus at position 0 mm. The total counts and the maximum endpoint energy decreased as the target was moved farther from the center. This experiment verified that the optics did focus the beam, however it did not demonstrate the 100 keV goal.

4.3 Optimized Experiment

This section presents all of the results obtained from the optimized configuration of the piezoelectric crystal x-ray source. These results demonstrated that the piezoelectric transformer could produce output voltages greater than 100 kV, exceeding requirements for a compact x-ray source (40−60 kV) and the threshold for the D(d,n)^{3}He nuclear reaction. A time-dependent effect of x-ray production was discovered and a series of experiments was developed to investigate this effect. Five parameters were selected as treatment variables to test both the maximum voltage of the piezoelectric crystals and the rate of x-ray production over time. A total of 58 observations were made in this investigation and raw data from each observation have been included in Appendix A.

4.3.1 Early Results

The optimized configuration for x-ray production was the first method which produced x-rays above 100 keV in this experiment. The crystal was painted in the Rosen configuration and the crystal output was directed towards a 50 μm-thick aluminum x-ray window installed on a vacuum chamber port. The CdTe detector was positioned outside the chamber adjacent to the aluminum window. The spectrum associated with this first high voltage measurement is shown in Fig. 4.6.

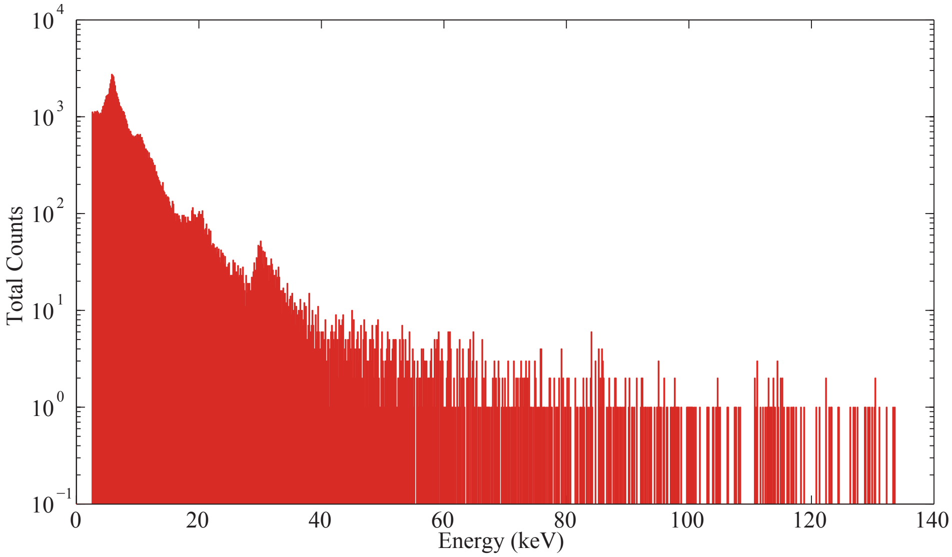

Figure 4.6: First recorded x-ray spectrum from a piezoelectric crystal showing x-ray energies greater than 100 keV.

The validity of the measurement shown in Fig. 4.6 is supported by the presence of multiple fluorescence peaks. These peaks correspond to characteristic x-ray fluorescence energies of materials known to be present in the vacuum chamber. Several x-ray peaks are visible in the spectrum shown in Fig. 4.6 including the iron k-α peak at 6.4 keV and the silver k-α peak at 22.16 keV. Table 4.1 summarizes the peaks in the spectrum from Fig. 4.6 and their possible sources.

Table 4.1: X-ray fluorescence peak list for spectrum in Fig.4.6

Peak Energy(keV)	Element(s)	Designation	Source Description
6.4	Fe	K-α	Iron in steel chamber walls
10−12	Pt, Ir	LM-β, LN-γ	Field emitters
22.16	Ag	K-α	Paint at crystal output
28.7−29.2	Sn	K-β	Solder on circuit board

Pulse pile-up is another characteristic that must be considered to ensure the validity of x-ray spectra. Pile-up is caused by the additive effect of simultaneous low energy incident radiations falsely registering as a single high energy x-ray count. The threshold for this effect is dictated by the pulse processing hardware and software. The Amptek MCA used in this experiment had a 0.6 μs fast channel resolving time, meaning that the spectrum was at risk of pile-up when two counts occurred within 0.6 μs of one another. This corresponds to a count rate of 1.67×10^6 counts per second. The maximum count rate recorded in any observation was 2,475 counts per second, indicating a low to nonexistent risk for pile-up throughout the experiment. Since pile-up was not likely to occur, the counts measured at 130 keV are a genuine representation of the true x-ray output of the piezoelectric transformer.

Figure 4.7 shows the same spectrum from 4.6 in a binned format. Error bars correspond to ± one standard deviation of the counts per bin. Figure 4.7 has 10 discrete energy bins with each bin containing the combined counts of approximately

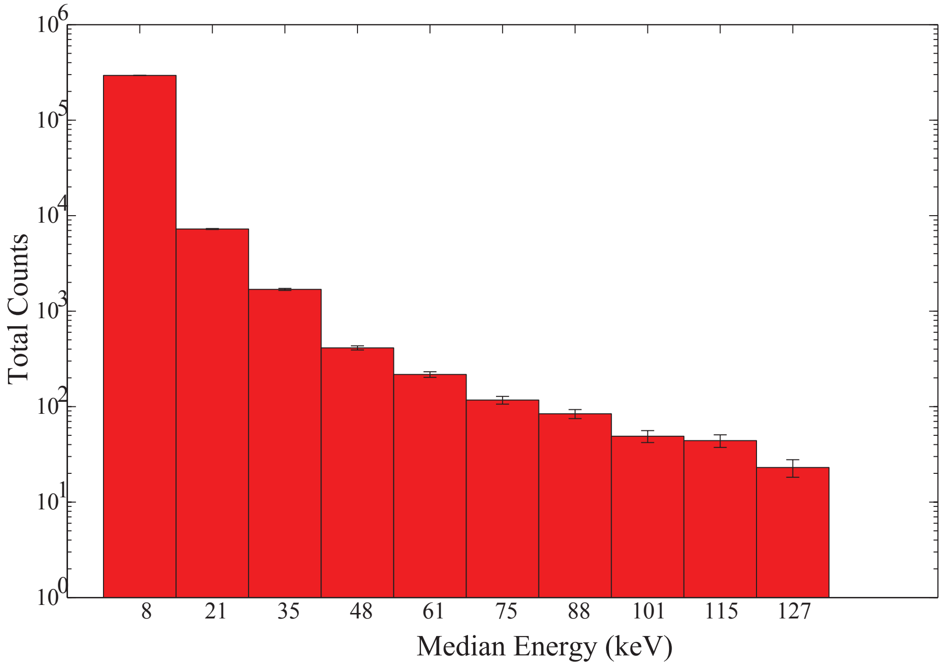

Figure 4.7: Same spectral data from Fig. 4.6 presented in a binned format.

100 channels. The term *median energy* on the x-axis of Fig. 4.7 refers to the energy associated with the channel in the middle of each bin.

It was discovered that x-ray count rate and endpoint energy both decreased as runtime increased. This limited data collection to approximately 1 minute of livetime. Figure 4.8 shows the total counts collected within two successive 60-second time periods. Spectral trends such as the iron k_α peak at 6.4 keV were visible at both sampling times, but counts in the second period were two orders of magnitude lower than the first period. The endpoint energy in the first period was 127 keV but decreased to about 15 keV in the following period.

The analysis presented in Fig. 4.8 is the first documented account of the time-dependent decrease in endpoint energy and count rate. One explanation for this effect is that the emitters were damaged during operation due to a blunting effect. Another

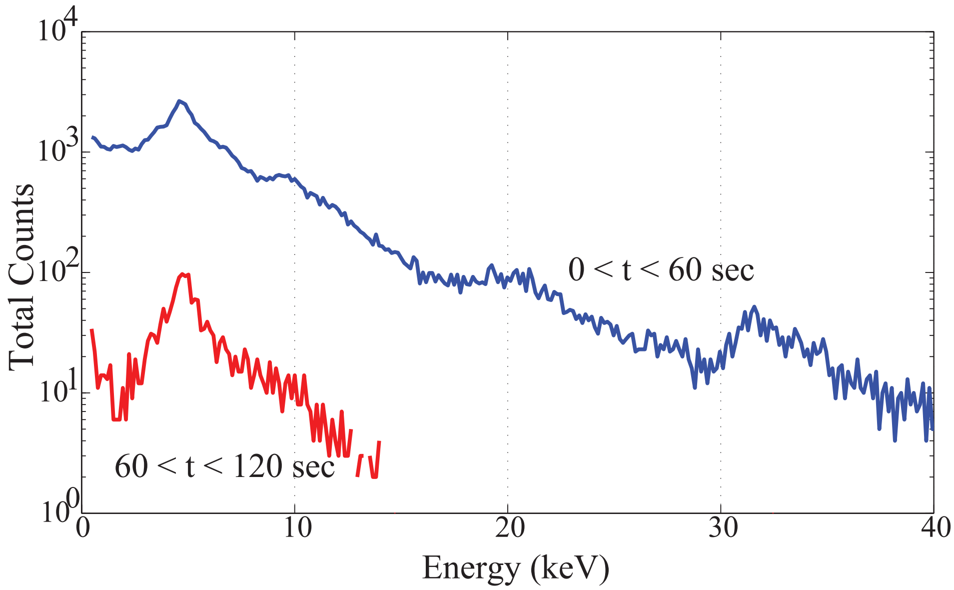

Figure 4.8: Same spectrum from early optimized configuration spectrum presented in total counts to demonstrate time-dependent count rate reduction

explanation is that, with no current return path, the the available free charge at the crystal output was depleted by the electron beam.

Field emitters must satisfy a number of requirements in order to operate effectively. Particularly, emitter material strength and melting point must be above a certain threshold. The PtIr wire manufacturer recommends the product for high field enhancement applications, and a brief analysis will confirm this claim [45]. Field emitters must be able to withstand stresses of at least 100 Mpa and temperatures up to 1300 K [23]. Platinum does satisfy these conditions with a tensile strength between 125−240 Mpa and a melting point of 2041 K.

While the PtIr emitters meet the material requirements for an effective field emitter, the operating and vacuum conditions during the experiment were not ideal for sustained electron emission. It is recommended for field emitters to be cleaned by electrical heating in vacuum to evaporate contaminants. This process was never implemented during experimentation, so it is possible that surface contaminants limited emitter current. Additionally, operating at vacuum pressures of 10^{-7} Torr or greater is known to decrease emitter lifetime. This process occurs in two ways. First, the impingement of charged gas molecules on the emitter surface leads to the formation of atomic monolayers. At a pressure of 10^{-7} Torr, 10^{15} $^{\#}/_{\mathrm{s}\cdot\mathrm{cm}^2}$ impinge on the emitter surface, and with adhesion ratio of $0.1-0.01$, a monolayer can form within $10-100$ seconds of operation. Second, ion bombardment causes localized pits and crests to form on the emitter surface, resulting in increased local field enhancement at the crests. This initiates a positive feedback cycle in which the increased field enhancement at the crests causes increased ion bombardment rates, further increasing the height and quantity of the crests. If this process is permitted to continue, the emitter is eventually destroyed by vacuum arcing [23]. Monolayer formation and ion bombardment are effectively mitigated by operating at 10^{-9} Torr or higher, however, this level of vacuum was not achievable by the available vacuum hardware, therefore short emitter lifetime was an unavoidable aspect of the experiment.

A alternative argument to the degradation of emitter quality for the time dependent decrease in x-ray count rate is that the electron beam depleted charge from the output of the crystal. Since a current return path was not provided to the output of the crystal, charge could not be replenished during the positive half-cycles. Due to the vey low capacitance between the crystal output and chamber walls, even a small drop in charge was reflected by a substantial drop in voltage. The following analysis investigates this phenomenon.

A combination of energy conservation laws and Fowler-Nordheim (FN) analysis is used to determine the maximum amount of charge that could be emitted from the crystal in one half-cycle of operation. First, the input power to the crystal is calculated by multiplying the input voltage and current sinusoids. The peak input power is 896 mW, meaning that the output power cannot exceed this value. Figure 4.9

shows the input and output power for the crystal for one half-cycle of 125 keV crystal operation.

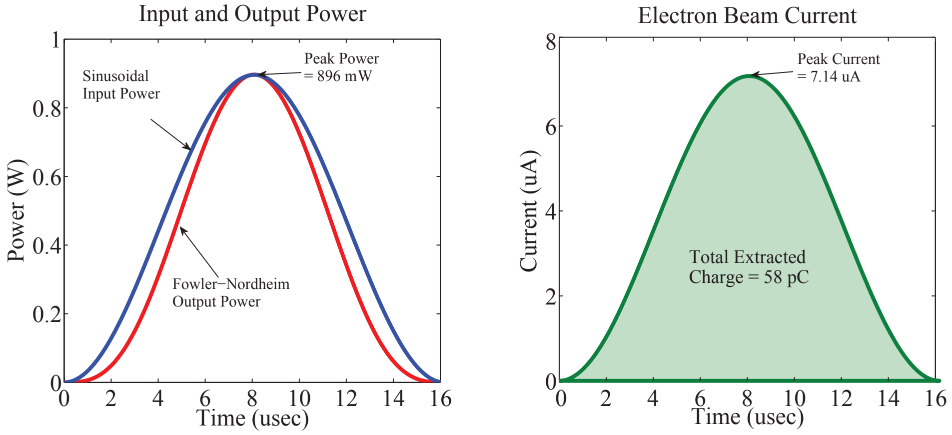

Figure 4.9: Input and output power to the crystal and the maximum charge extracted from crystal in one cycle at 125 keV output voltage

The FN equation is used to determine the output current when constrained to 896 mW. The FN equation is shown in Eq. 4.1.

$$\begin{aligned} J_{FN} &= A_{FN}(\beta V)^2 exp\left[\frac{-B_{FN}\phi_w^{3/2}}{\beta V}\right](A/cm^2) \\ A_{FN} &= 1.42\times 10^{-6}\frac{1}{\phi_w}exp\left[\frac{10.4}{\phi_w^{1/2}}\right] \\ B_{FN} &= 6.44\times 10^{-7} \end{aligned} \tag{4.1}$$

The values J_{FN}, β, V, and ϕ_w refer to the electron beam current density in A/cm^2, the field enhancement factor, the output voltage in V, and the metal work function in eV. The value for V is known from the x-ray voltage diagnostic to be 125 kV and ϕ_w is known from the material properties of platinum to be 5.2 eV. The value for β is not known with precision, however values range from 1−1000, largely depending on geometry and fabrication conditions [27]. Since β is not directly known, a value is selected such that the maximum amount of current is delivered without surpassing the input power of 896 mW. The value for β is set to 18.7 to produce the output power and current plots from Fig. 4.9. Above this value, the current cannot increase any further since it is limited by the input power. Figure 4.9 shows that for a crystal with five PtIr emitters, each with an emission area of 1 nm^2, the output beam current reaches a maximum of 7.14 μA, extracting a total of 58 pC in one half-cycle.

Using the equation for capacitance, shown in Eq. 4.2, a relationship between the change in charge and drop in output voltage can be computed.

$$\Delta V = \frac{\Delta Q}{C} \tag{4.2}$$

Equation 4.2 shows that as the charge separated by a fixed capacitance decreases, the voltage across that capacitance must also decrease. The output capacitance of the crystal is largely due to stray capacitance between the crystal output and the vacuum chamber walls and has been determined to be between 0.1−1 pF [46]. Solving for ΔV with $\Delta Q = 58$ pC and C = 0.1 pF yields a drop of 580 V in the first negative half-cycle of. A current return path was not provided to the output, so charge was not reclaimed during the positive half-cycle. The 580 V drop at the output remained until the beginning of the next negative half-cycle. Since the FN equation is highly dependent on output voltage, the drop in voltage caused a reduced output current and less charge was extracted. This degenerative sequence of voltage and current drops rapidly reduced the maximum achievable voltage by the crystal. A finite-difference time-domain (FDTD) model was used to compute the drop in output voltage for a range of output capacitances. The FDTD results are shown in fig. 4.10.

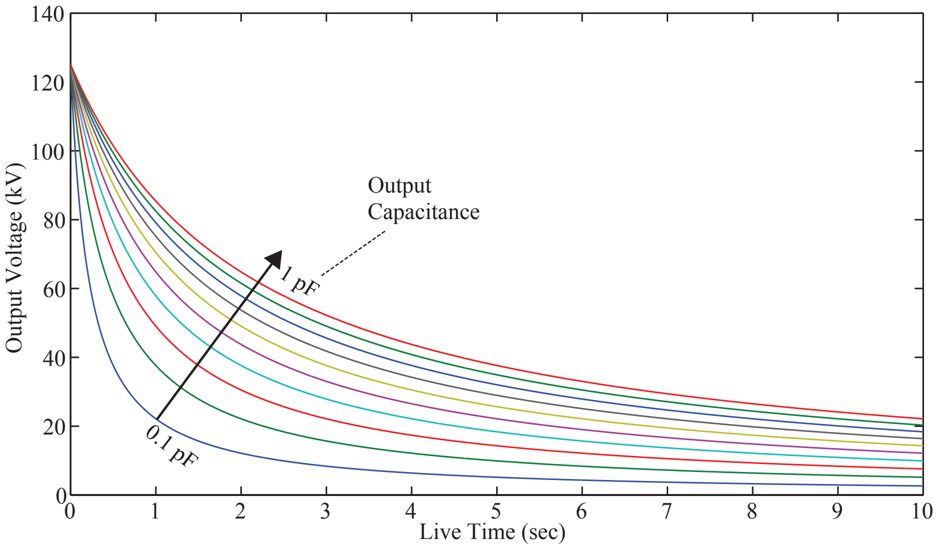

Figure 4.10: Time-dependent decrease in output voltage due to charging for a range of crystal output capacitances.

Figure 4.10 shows the rapid decrease in output voltage as live-time increases. Each second corresponds to 1000 cycles. The output capacitance was varied between 0.1−1 pF in steps of 0.1 pF. Output capacitance was inversely related to the rate of change of voltage. Higher capacitances resulted in less charge emitted per burst and the crystal voltage dropped more slowly. As capacitance decreased, the voltage drop occurred more quickly. After one second, the output voltage was approximately 80 kV for 1 pF and 20 keV for 0.1 pF. After ten seconds, the change in voltage had reduced for all capacitances, but the output voltage dropped to between 5−20 kV. This model indicated that the charging mechanism was likely to limit the amount of time that the piezoelectric crystal could produce high voltage. The effect of charging could be reduced by incorporating a current return path to the output or increasing the crystal output capacitance.

Both the emitter degradation and crystal output charging mechanisms are plausible explanations for the time dependent decrease in x-ray count rate. Comparison between emitter characteristics from literature and the operating conditions of the experiment indicate the there was a high likelihood that the emitters were being destroyed when energized. Additionally, Fowler-Nordheim analysis suggests that charge extraction rapidly reduces the output voltage of the crystal. The combined effects of both mechanisms would greatly limit the x-ray flux as time increased. Experimental results in the following section physically investigate this effect and provide evidence to support the claim that the emitters were degraded during operation.

4.3.2 Parametric Investigation Results

A parametric sweep of piezoelectric crystal operating conditions was conducted. The variables were crystal sample, number of emitters at the crystal output, duty cycle, and pressure of the vacuum chamber. Time-resolved data was collected during each experiment to monitor when high energy counts occurred. A gate signal synchronized MCA live-time with resonant bursts to the crystal to increase x-ray signal-to-noise ratio.

First, the individual crystals were tested to verify consistent high voltage performance among samples. Each crystal was manufactured with a tolerance of $\pm 0.2\,\text{mm}$ and electrodes were applied consistently as described in section 3.2.1. Due to the manufacturing tolerances of the crystal fabrication process and preparation technique, each crystal sample was expected to produce similar high energy x-rays and count rates.

The number of emitters present at the output of the crystal was varied to investigate its effect on endpoint energy. An increased number of emitters present at the output would permit the crystal to produce more electron current by increasing the surface area at the tips exposed to high fields. By increasing the electron current, probability of measuring x-rays is improved and more high-energy x-ray counts are anticipated.

The duty cycle of the crystal was investigated to determine if a varied burst period affected the endpoint energy. Previous testing had indicated that burst periods of less than one second would result in crystal fracture, so the minimum burst period for this experiment was fixed at 1 second. A burst period of 2 seconds was tested and compared to the 1 second period case.

The vacuum pressure was investigated because the piezoelectric crystal is to eventually be used in a low pressure ($0.5-1\,\mathrm{mTorr}$) deuterium environment. As the pressure increased from high vacuum, the electric field strength necessary for breakdown in vacuum decreased in accordance with the Paschen Law. Electrical breakdown was undesirable because discharges on the crystal surface electrically load the crystal, limiting its ability to reach high voltage. The hypothesis was that there is a maximum pressure above which the crystal can no longer produce high energy x-rays.

4.3.2.1 Crystal Sample

The first parameter that was investigated was the effect of the crystal sample itself on the maximum achievable voltage. The crystals were manufactured with a tolerance of $\pm\,0.2\,\mathrm{mm}$ which was not enough of a difference to significantly effect the output voltage due to the linear relationship between crystal length and gain, as described by equation 1.4. Additionally, each crystal was painted in a consistent manner using the methods described in section 3.2.1. Considering the physical consistency among the crystal samples, each crystal was expected to perform similarly. The results from the crystal sample experiment are shown in Fig. 4.11.

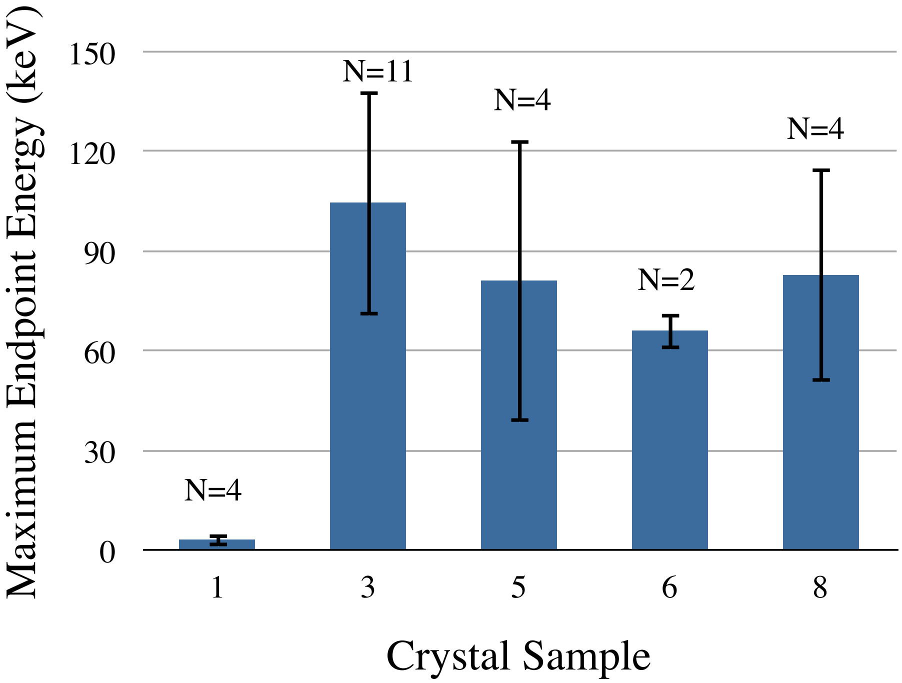

Figure 4.11: Effect of crystal sample on endpoint energy. Burst period = 1, 2 s; Number of emitters = 3−5

The crystal sample number was assigned arbitrarily in a logbook of crystal history. Five different crystal samples were included in the experiment. Crystal 3 consistently performed with the highest output voltages. Crystal 1 is the only sample which never reached a high output voltage, even though it was prepared similarly to the other samples. Crystals 5, 6, and 8 all produced high energy x-rays, but their performance cannot be statistically distinguished because of the high standard deviation of the measurements. Variability in crystal constituent parameters like micro-cracks and electrode thickness and conductivity may have contributed to the discrepancy in crystal output voltage.

4.3.2.2 Number of Emitters

An investigation into the effect of emitters at the crystal output was conducted. A number of tests were conducted to collect sufficient data on the effect, as PtIr emitters were periodically lost during the experiment. A maximum of five emitters could be reliably adhered to the crystal output, setting the upper limit of the treatment. The lower limit of the treatment was selected to be zero emitters to set a control for the effect. The results of the emitter experiment are shown in Fig. 4.12.

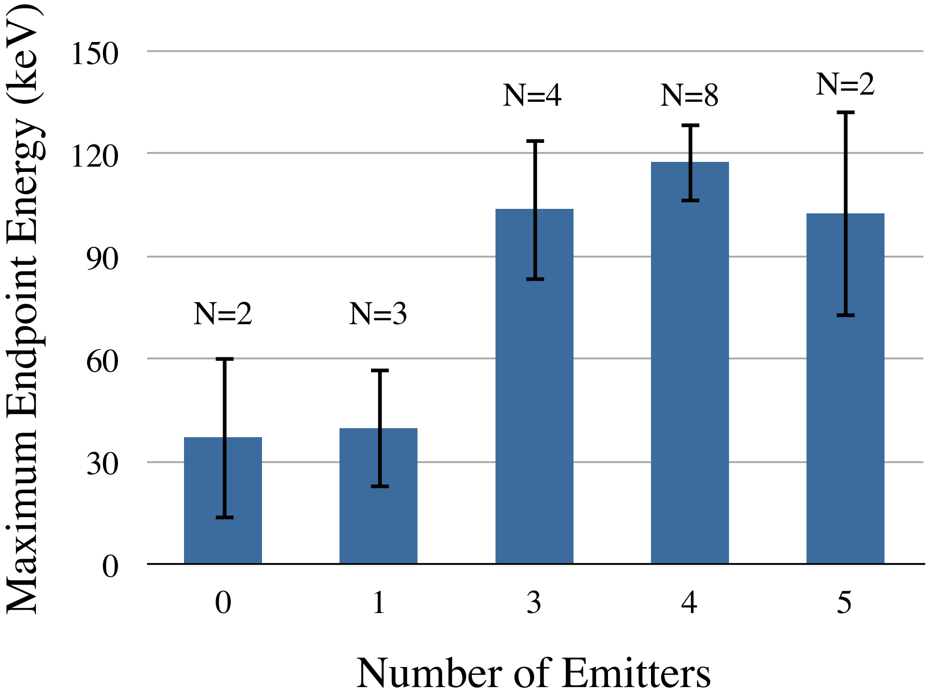

Figure 4.12: Effect of number of emitters on endpoint energy. Pressure = 10^{-6} Torr; sample = crystal 3; Burst period = 1 s

A total of 19 observations were included in this experiment. The number of observations N at each treatment level is shown in Fig. 4.12. As can be seen in Fig. 4.12, the number of emitters is significant. In the zero- and one-emitter cases, a mean endpoint energy of approximately 40 keV was observed. When the number of emitters was increased to between three and five, the mean endpoint energy increased to approximately 100 keV. Error bars correspond to one standard deviation of the mean in each case.

4.3.2.3 Duty Cycle

The effect of duty cycle on endpoint energy was investigated. Duty cycle is a function of burst length and burst period, however burst length was fixed in all experiments. Maximum resonance typically occurs after 2000 cycles when the peak to peak current no longer increases in time. A burst of 3000 cycles was chosen as a standard setting to permit 1000 cycles of sustained high resonance operation. Since the frequency and cycles per burst were both fixed, the duty cycle experiment specifically investigated the effect of burst period.

Burst periods of one and two seconds were investigated in this experiment. The effect of background was constant in both cases because a gate signal was used to ignore counts accumulated during crystal dead-time. Pressure, number of emitters, and crystal sample were held constant. The results from the duty cycle experiment are shown in Fig. 4.13.

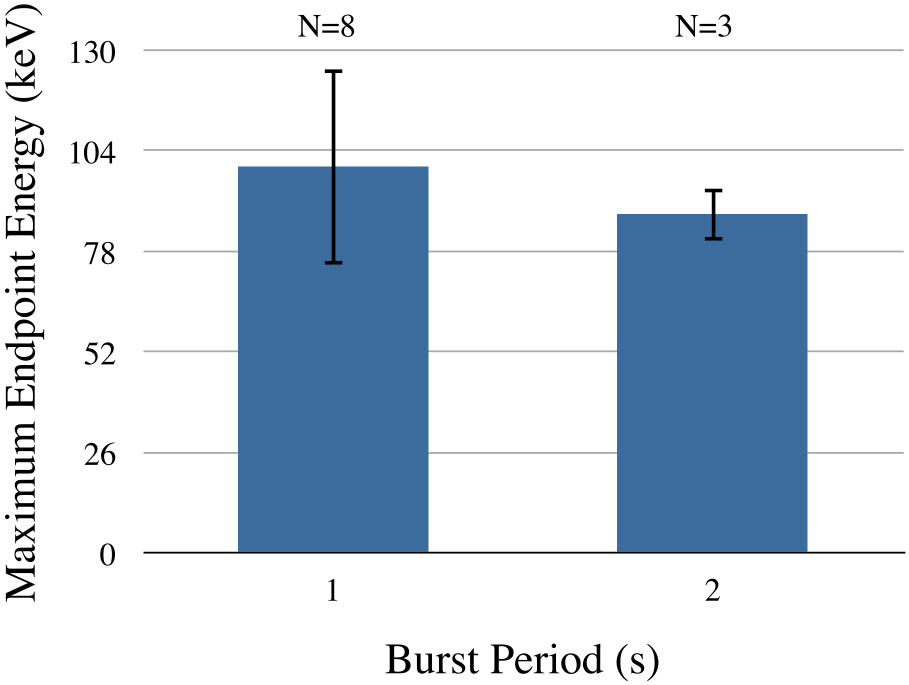

Figure 4.13: Effect of burst period on endpoint x-ray energy. Pressure = 10^{-6} Torr; sample = crystal 3; Number of emitters = 5

Figure 4.13 shows that there is no significant effect of burst period on the maximum output voltage of the crystal. The usable data set for the two second burst period was limited to three observations due to tip loss during operation. Since there was no significant effect of burst period on maximum output voltage, a burst period of one second was preferable to reduce data collection times.

4.3.2.4 Pressure

The effect of pressure on the maximum voltage of a crystal was investigated to identify operating pressure limits. The experiment investigated four pressures: $5{\times}10^{-6}$, $5{\times}10^{-5}$, $5{\times}10^{-4}$, and $5{\times}10^{-3}$ Torr. The results for the pressure experiment are shown in Fig. 4.14.

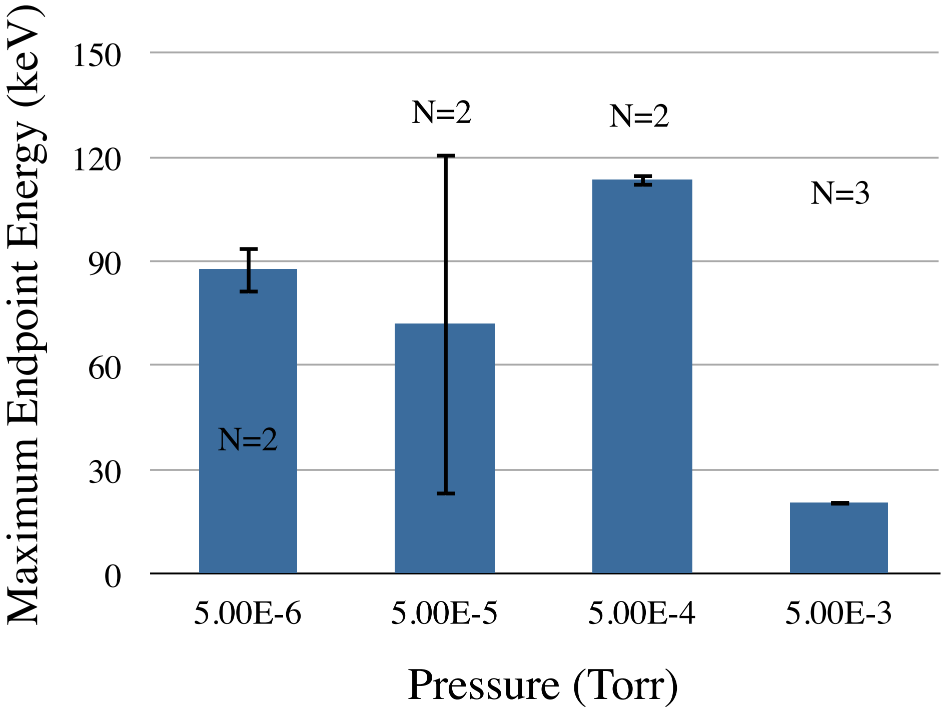

Figure 4.14: Effect of pressure on average maximum x-ray energy. Burst period = 1, 2 s; sample = crystals 5, 8 Number of emitters = 3−5

Both the 3-, 4-, and 5-emitter cases and the one- and two- second burst period observations were combined to increase the number of observations. This approach is valid because results from sections 4.3.2.2 and 4.3.2.3 indicated no significant effect among these treatments.

Figure. 4.14, shows that a pressure of $5{\times}10^{-3}$ Torr greatly limits the maximum x-ray energy produced by the crystal. The other three pressures did not limit x-ray energy; however the error bars for the $5{\times}10^{-5}$ Torr were much larger than any other case. Crystals 5 and 8 were used in the $5{\times}10^{-5}$Torr case, however data from section 4.3.2.1 showed that these two samples reached the same mean endpoint energy. Since the controlled variables between the two observations for the $5{\times}10^{-5}$Torr case showed no effect on endpoint energy, the large error bar at $5{\times}10^{-5}$Torr was likely due to an uncontrolled variable.

4.3.3 Time-Dependent Effects

The time-dependent output of the piezoelectric crystal was found during the optimized configuration testing. A difference in x-ray count rate with respect to time, particularly in the high energy region, was observed during testing. This phenomenon, discussed in section 4.3.1, was investigated throughout the parametric investigation of the crystal by collecting time-resolved data. A Matlab script was used to parse data from these spectra to isolate the counts produced during each time interval [47]. Data from 15 spectra are shown in Fig. 4.15 that show an effect on the number of emitters on the timing of high-energy x-ray production.

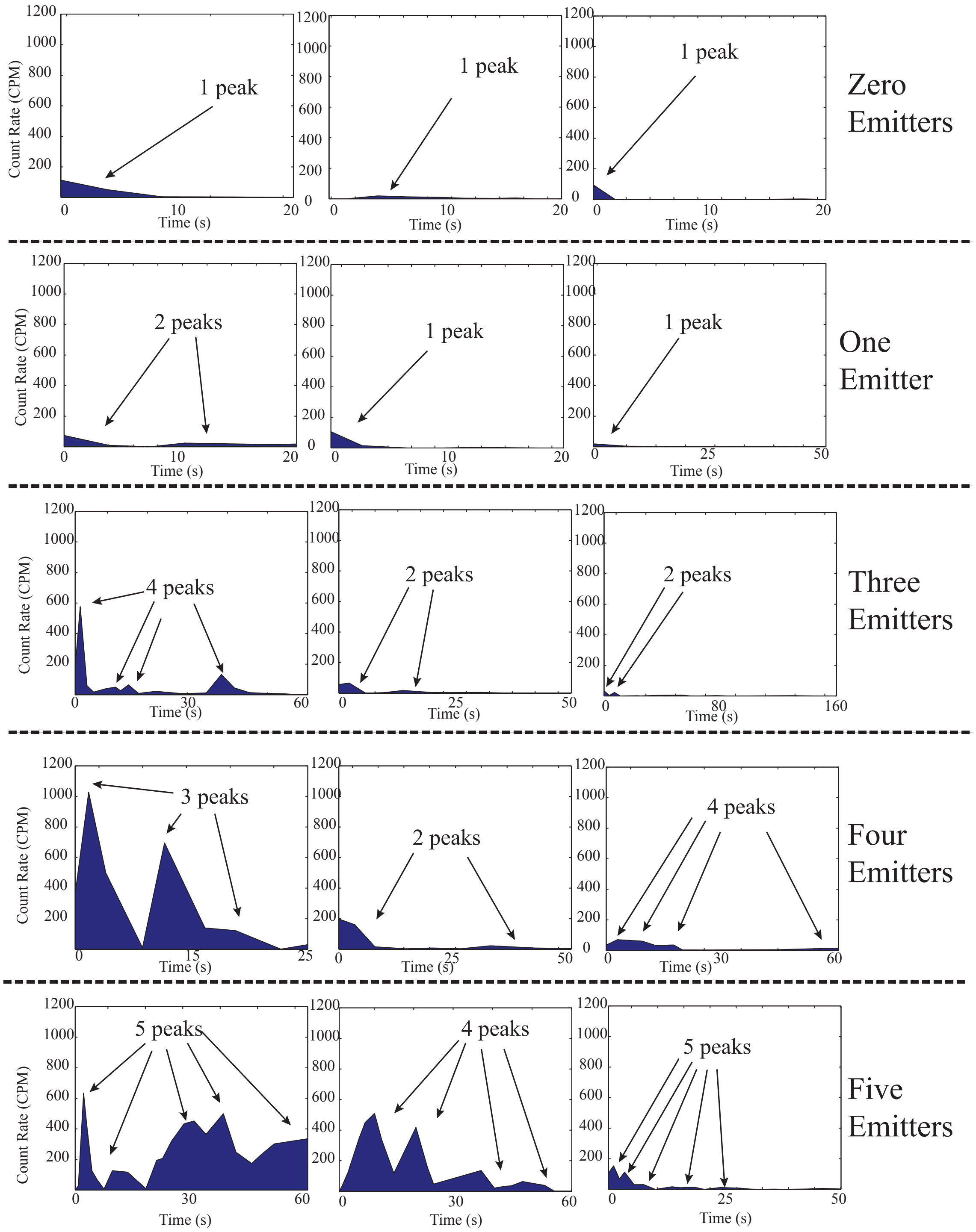

Figure 4.15: Time-resolved count rates as the number of emitters increases. Thee observations per treatment level are shown. Peaks correspond to the destruction emission points due to monolayer formation and vacuum arcing.

Figure 4.15 shows time-resolved x-ray count data for the five treatment levels of the emitter number experiment. Only x-rays with energy greater the 30 keV are shown. Each sub-figure corresponds to an individual run of the crystal. Three observations per number of emitter show the variation among observations at each level. This figure demonstrates that peaks of x-ray count rates occurred throughout the duration of a test. Specifically, it shows how the number of these peaks increased as the number of emitters on the crystal increased. In the zero- and one-emitter cases, only one or two peaks appeared and the count rates were relatively low (~ 100 CPM). The number of peaks and maximum count rates increased with the number of emitters, reaching $3-5$ peaks per test and count rates up to 1000 CPM.

Considering the analysis presented in section 4.3.1, it is possible that these peaks were due to the destruction of individual emitters by the accumulation of atomic monolayers and ion bombardment. In each test, the first peak was the most prominent and in general, the height of subsequent peaks decreased. When more emitters were added to the crystal, the likelihood of having an emitter with a high field enhancement increased. When the crystal reached high voltage, the emitters were sequentially energized and began emitting one after another. As one emitter was destroyed due to the degradation mechanisms described in section 4.3.1, another emitter began emitting beam current. This process continued until all emitters had been destroyed. In the case of zero emitters, peaks were still present. These peaks could be produced by the lithium niobate itself emitting charge due to field enhancement at the corners of the crystal.

The data presented in Fig. 4.15 demonstrate a trend in the distribution of count rates over time. The destruction of emitters is a plausible explanation for this effect because emitters are known to be susceptible to damage when operated at pressures of

10^{-6} Torr. The number of peaks increased with the number of emitters, supporting the claim that the two parameters are related. The problem of emitters being destroyed during the experiment needs to be solved if extended periods of high voltage operation are desired. Literature suggests that a vacuum pressure of 10^{-9} Torr or higher will provide a safe environment for the emitters. Another option would be to abandon the use of electron emitters and develop another method for extracting energy from the piezoelectric crystal.

4.4 Plasma Generator Results

The plasma generator experiment showed that the dual Rosen configuration was an effective way to produce an rf plasma. The outputs of two crystals were placed in an overlapping fashion on a circuit board and were driven to resonance simultaneously using two different rf sources. Deuterium gas was flowed into the chamber over a range of pressures and a digital camera was used to image the plasma. The CdTe x-ray diagnostic was used throughout the experiment to monitor the output voltage of the generator.

The plasma generator pressure was swept between 9 mTorr and 25 mTorr. At pressures below 9 mTorr, no plasma was visible using the digital camera. At pressures above 25 mTorr, the crystal resonant frequency became unstable, preventing controlled operation of the generator. The resonance instability increased as the pressure exceeded 25 mTorr, therefore the pressure scan was terminated at this pressure.

Figure 4.16 shows the imaging results of the plasma generator at eight different pressures. The left column shows a plot profile of the plasma, showing the vertically averaged pixel intensity as a function of horizontal distance across the gap. Pixel intensity is reported in grey values between 0 and 255 with 0 corresponding to no exposure of the pixel and 255 corresponding to complete exposure. Plotting this intensity showed where the plasma formed within the gap and in what relative quantity. As the pressure increased, a peak of intensity appeared within the region directly between the output of the two crystals (between 2.5 and 3 cm). In addition to a more pronounced intensity peak, the background level of intensity increased as well. This suggests that increasing amounts of plasma were filling the vicinity immediately surrounding the gap as the pressure increased.

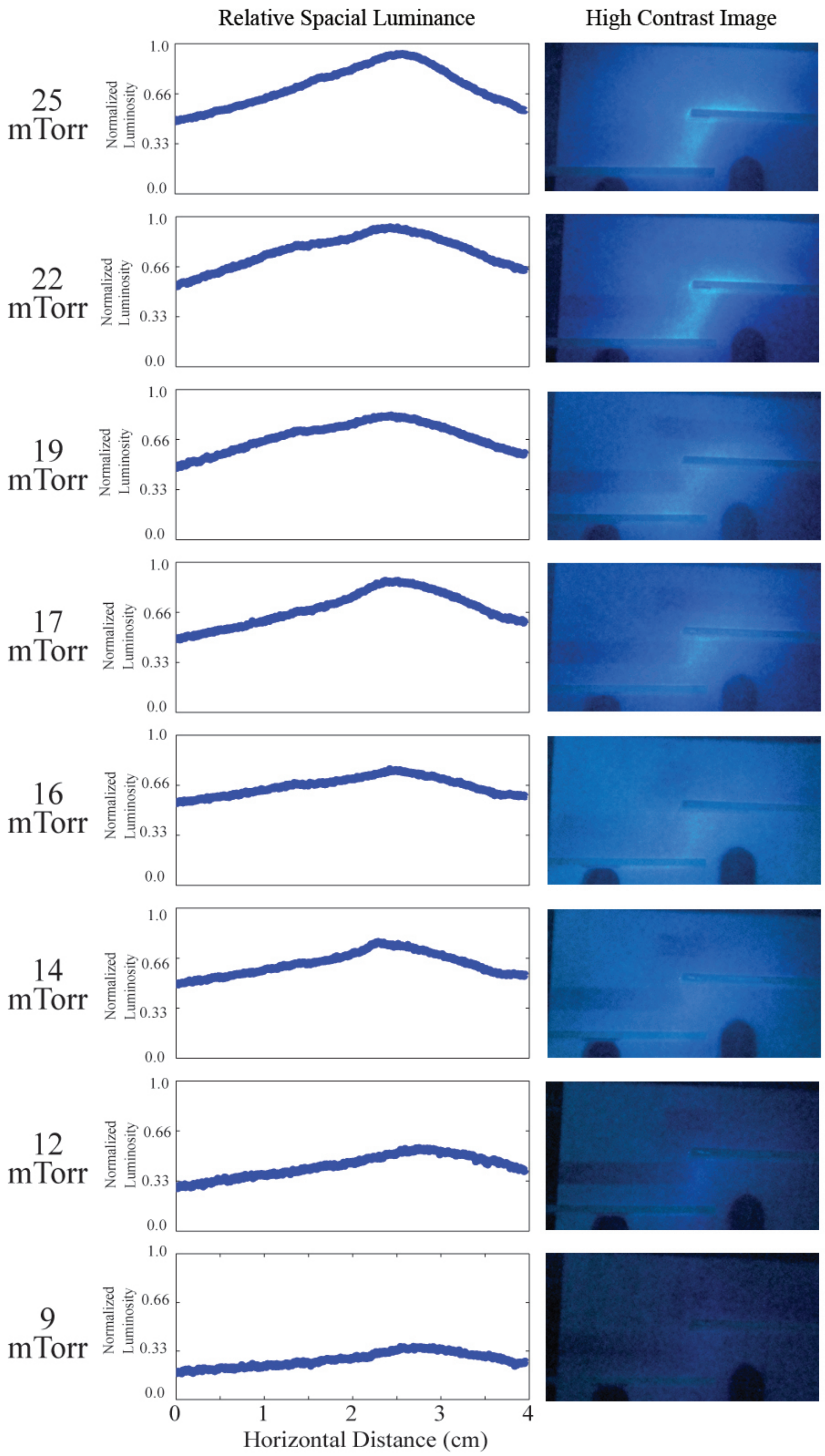

Figure 4.16: Relative luminance of plasma with varying pressures of deuterium gas.

To accompany the plot profile, digital images of the plasma have been included in Fig. 4.16 as well. At 9 mTorr, the plasma was quite dark. As the pressure increased, so did the light emitted from the plasma. At 16 mTorr, a concentrated plume of plasma became visible between the two crystals which increased in brightness with pressure. This plume was approximately 50 % brighter than the surrounding plasma at each pressure, which can be seen by comparing the grey values at center of the plume ($x \simeq 2.75$ cm) to the grey values 0.5 cm away on either side of the plume in the plot profile column.

The photons produced by the plasma were not directly counted because the digital camera is not calibrated for this kind of measurement. Overall luminosity can be inferred, however, by integrating grey values over the horizontal gap distance, yielding the total grey value. Figure. 4.17 shows the luminosity integrated over 4 cm of horizontal distance (1544 pixels) for each pressure. The relative amount of plasma generated at each pressure can be crudely compared using this method. The plasma at 9 mTorr was 40 %. This increased to 9 % at 16 mTorr, and reached a unity at 22 mTorr. The plasma decreased to 9 % at 25 mTorr because the resonance became unstable and produced less plasma as a result.

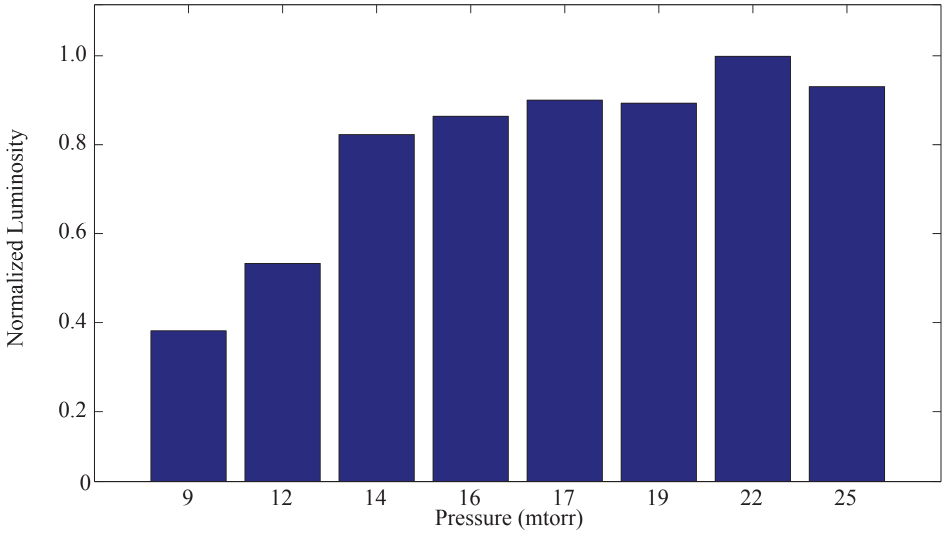

Figure 4.17: Relative amount of plasma at each pressure.

X-ray data was collected from the experiment as well, however, x-rays were only measured at the lowest pressure level. At 9 mTorr, bremsstrahlung x-rays with energies up to 125 keV were detected, indicating that the voltage between the two crystals was at least 125 kV. The detector was not calibrated for x-rays higher than 125 keV, so the maximum measurable endpoint terminated at this energy. Figure 4.18 shows the x-ray spectrum collected from the plasma generator at 9 mTorr.

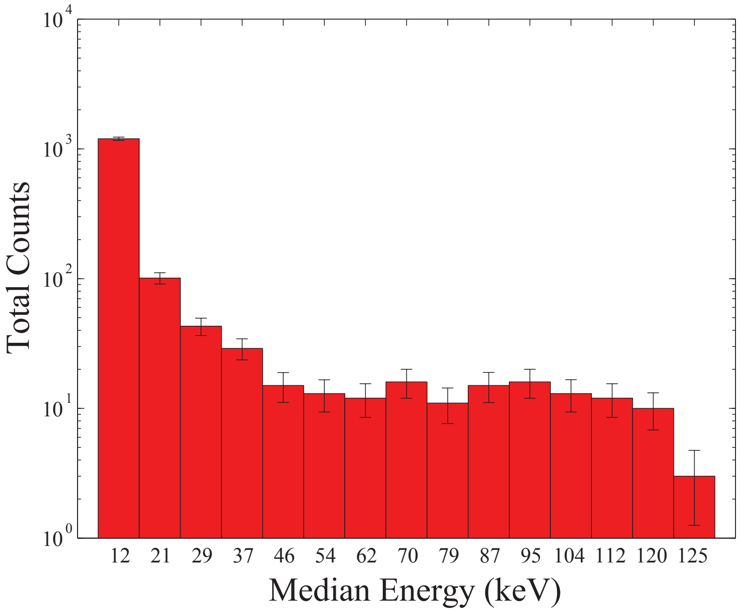

Figure 4.18: Binned bremsstrahlung x-ray xpectrum for 9 mTorr run.

The x-ray spectrum produced by the plasma generator shows a continuous x-ray spectrum reaching an endpoint energy of 125 keV using zero emitters. These results contrast with the results obtained in section 4.3.2.2 where it was shown that in the zero emitter case, a maximum energy of only 40 keV was observed. The endpoint energies are different in theses two cases because two different mechanisms are used to produce electron current. In the case of the emitters, field emission produces electron current by extracting electron charge from the emitters and crystal surface. When no emitters are present on the crystal, the field enhancement factor is reduced and the amount of electron current that the crystal can produce drops as a result. In the case of the plasma generator experiment, electrons are produced when deuterium gas atoms are ionized by the electric fields between the two crystals. Since the electrons are sourced by the gas and not the surface of the crystal, no emitters are necessary to produce electron current and high energy bremsstrahlung x-ray radiation is observed.

It was also observed that of all of the pressures investigated, x-rays were only produced in the 9 mTorr case. Figure 4.17 showed that more plasma was produced as the pressure increased from 9 mTorr, however the x-ray production immediately ceased when the pressure was increased above 9 mTorr. This effect indicated that one of two mechanisms was taking place: either the voltage of the generator dropped below a detectable magnitude or the electron current never interacted with a metallic target to produce x-rays.

One mechanism to explain the halting of x-ray production at 12 mTorr is that the output voltage of the plasma generator dropped below detectable levels. The lower level discriminator for the MCA was set to 8.6 keV to reject noise and low energy x-ray counts. Industry rf plasma sources typically operate at drive voltages of $100-1000$ V with a plate separation of $2-10$ cm, at pressures between $10-100$ mTorr and power densities between $0.1-1$ W/cm^2 [48]. These conditions are very similar to the operating conditions of the piezoelectric plasma generator, therefore it is reasonable to conclude that the output voltage of the generator could drop below 8.6 keV yet still be capable of producing plasma.

The drop in voltage is due to the resistive loading on the output of the piezoelectric crystal caused by the plasma. As the plasma density increases, so does the current necessary to sustain it. The piezoelectric crystal is a voltage transformer and the conservation of energy dictates that the output power of the crystal must not exceed the input power. Since input power, voltage, and current are essentially fixed by the rf drive sources, the output current is fundamentally limited to the input current divided by the crystal voltage gain. Tables 4.2 and 4.3 contain analysis of the power consumption and maximum output current of the plasma generator while operating at full voltage gain.

Table 4.2: Plasma generator power

	Piezo 1	Piezo 2	
V_{max}(V)	11.2	11.2	Input
I_{max}(mA)	40	70	
V_{RMS}(V)	7.91	7.91	
I_{RMS}(mA)	28.2	49.5	
P(mW)	223	392	
P_{total}(mW)	615		

Table 4.3: Maximum deliverable current for plasma generator under full voltage gain for experimental and theoretical output voltages. Current is calculated from power as determined in Table 4.2 (100 % efficiency assumed)

	Experimental	Theoretical	
V_{max}(kV)	125	250	Output
V_{RMS}(kV)	88.4	176.8	
I_{RMS}(μA)	6.96	3.48	
I_{max}(μA)	9.84	4.92	

Table 4.2 shows that the total power consumed by the plasma generator was 615 mW. This power is the combined power to drive both piezoelectric crystals (labeled *Piezo 1* and *Piezo 2*). Voltage and current values are given in amplitude and RMS values to aid in direct calculation of power. Table 4.3 shows the maximum deliverable current of the plasma generator which was calculated by dividing the power as determined in Table 4.2 by the output RMS voltage of the generator assuming 100 % transformation efficiency. The experimental column uses 125 keV as the output voltage, the maximum measured voltage of the plasma generator. The theoretical column uses 250 keV as the output voltage, which is twice the measured voltage of a single crystal from experiments conducted in Section 4.3. The theoretical column therefore describes the current capabilities of the generator under the most current-restricted case (each crystal operating at 125 keV).

A rough estimate for the minimum current necessary to drive an industrial rf plasma diode can be calculated from the typical power and voltage values as previously discussed [48]. Choosing a maximum drive voltage of 1000 V (707 V_{RMS}) and minimum power of 0.1 W/cm^2 yields a current density of 200 μA/cm^2, representing the minimum current that would ever be used to drive an industrial plasma source. In the case of the piezoelectric plasma generator, current density is equivalent to current since the output electrode is 1 cm×1 cm. To provide an output current of 200 μA with the piezoelectric plasma generator would require a factor of 20 increase in current for the experimental case or a factor of 40 increase in current for the theoretical. In either case, an increase in current is permitted only by a reciprocal decrease in voltage gain. Ultimately, to drive a plasma with the piezoelectric plasma generator under the most current-deprived conditions reduced the voltage gain from 11.1 kV/V to 560 V/V, reducing the output voltage to 6.15 kV. If the current restrictions were relaxed, this output voltage would only decrease. Since the lower level discriminator was set to 8.6 keV, it is apparent why no x-rays were measured while the generator was producing plasma.

The conclusion that the output voltage of the generator decreased during plasma production could be disputed since a low energy x-ray measurement was never conducted. An alternative explanation for the halting of x-ray production could then be attributed to a decrease in electron mean free path as a result of increasing the pressure in the generator. This decrease would stop bremsstrahlung radiation by preventing electrons from impinging on the metallic anode surface due to atomic collisions within the anode-cathode (A-K) gap. The following analysis disproves this claim. First, equation 4.3 is used to calculate the mean free path of an electron traveling through a gas [49].

$$\lambda_e = \frac{kT}{\sqrt{2} \cdot \pi \cdot d^2 \cdot p} \tag{4.3}$$

The expressions λ_e, k, T, d, and p refer to the electron mean free path in m, the Boltzmann coefficient in J/K, temperature in K, atomic diameter of the gas in m, and pressure in pa, respectively. The deuterium atomic diameter is $d \cong 1.1 \times 10^{-10}$ m [50]. The Beer-Lambert law is used to determine the transmitted beam intensity and is shown in Eq. 4.4.

$$\frac{I}{I_0} = e^{-x/\lambda_e} \tag{4.4}$$

The fraction of electron beam current that is transmitted across the A-K gap is described by the ratio I/I_0 where I is the transmitted beam intensity and I_0 is the initial beam intensity. The expressions x and λ_e are the A-K gap distance in m and electron mean free path in m. The A-K separation was 1 cm. Table 4.4 shows pertinent values for the selected operating pressures for the plasma generator.

Table 4.4: Calculated mean free path and transmission ratios for the plasma generator for 1 cm A-K gap separation.

Pressure (mTorr)	Mean free path, λ_e (cm)	Transmission ratio, I/I_0
9	68.8	0.986
12	48.1	0.979
14	41.2	0.976
16	36.2	0.973
17	33.9	0.971
19	30.4	0.968
22	26.2	0.963
25	23.1	0.958

Calculated values for electron transmission ratios shown in Table 4.4 indicate that only a 2.8 % drop in transmission ratio occurs between the lowest and highest pressures. Furthermore, a drop of only 0.7 % occurs between 9 mTorr and 12 mTorr.

Recalling that x-ray detection decreased from significant counts across the full 125 keV spectrum to zero counts within the 9−12 mTorr transistion, it is clear that the drop mean free path is not a plausible explanation for this effect. Ruling out the change in mean free path as the pressure increased, it is reasonable to conclude that the output voltage of the generator dropped at pressures above 9 mTorr.

This experiment has demonstrated that piezoelectric crystals can be used to build plasma generators and characterized how such a generator operates under a range of pressures. The output voltage of the generator is highly sensitive to pressure and quickly decreases as the pressure increases. The amount of plasma produced by the generator increases with pressure until resonance instabilities prevent the piezoelectric crystals from resonating, thus ceasing the production of plasma.

Chapter 5

Conclusions

The presented experiments demonstrated that a piezoelectric transformer produced x-rays with energies up to 125 keV. These results confirmed that the piezoelectric effect is a viable mechanism for compact x-ray production. The piezoelectric transformer far surpassed conventional piezoelectric devices and was capable of meeting and exceeding the operating voltage of x-ray applications like tomography of between 40−60 kV. Additionally, the results demonstrated that the piezoelectric effect is a feasible mechanism for D(d,n)^{3}He neutron sources, which require at least 100 kV for a reasonable cross-section. While further development will be required to demonstrate neutron production using a piezoelectric transformer, the results showed that the piezoelectric effect has many potential applications beyond the scope of conventional piezoelectric devices.

Modeling was conducted using finite element software to simulate the piezoelectric transformer x-ray source. An eigenfrequency solver calculated the resonant frequencies of the crystal and a displacement plot was used to select the correct frequency for the length extensional resonant mode. The electrical and mechanical parameters of the crystal were characterized using a frequency domain study, showing that peak electric field and von Mises stress occur in the center of the bar and peak output voltage and mechanical displacement occur at the extremities. An input voltage was selected to maximize output voltage without excessively stressing the material and risking fracturing the device. Electron beam optics were designed with an electrostatic model which increased electron flux on target. This increase in flux would produce higher x-ray counts, thus increasing the viability of the piezoelectric transformer as an x-ray source.

Experimental configurations were presented to test the output characteristics of a piezoelectric transformer x-ray source. Each iteration of the experiment was designed to improve upon an aspect of the previous. Electron beam optics were introduced to increase electron flux and improve x-ray counts, and high efficiency detectors, combined with binning and gating provided improved data collection techniques. A parametric investigation of variables was designed to determine optimal operating conditions for the x-ray source. A piezoelectric plasma generator configuration was introduced to explore additional methods for high voltage and x-ray production.

The results demonstrated that the piezoelectric transformer was capable of producing a spectrum of x-rays up to an endpoint energy of 125 keV. These results indicating that the piezoelectric effect is a viable mechanism to drive MEMS-scale x-ray sources. Initial experiments verified that the piezoelectric transformer x-ray source concept was possible. Subsequent configurations improved upon the initial experiment with enhanced methods, diagnostics, and analysis techniques. The plasma generator was an alternative to field emission structures for electron production and was capable of producing x-rays up to 125 keV.

An unexpected phenomenon was discovered in which the x-ray detection rate from the piezoelectric transformer decreased as runtime increased. High energy x-rays mostly occurred within the first 10 seconds of operation and were rarely measured after 1 minute. While this effect revealed interesting physics, it was undesirable for two reasons. First, it greatly slowed the data acquisition process because the vacuum chamber had to be vented between each experiment. Second, the counting statistics were worsened as a result of low long-term count rates. This effect was investigated using time-resolved x-ray spectra and two hypotheses were presented to explain the observed effects.

The first hypothesis was that the field emitters were being destroyed in each experiment. A study of literature on field emission structures indicated that emitters can be damaged at pressures above 10^{-7} Torr. Plotting x-ray count rate over time showed that abrupt peaks of x-ray counts occurred throughout the experiment runtimes. The number of peaks tended to increase with the number of emitters, suggesting that the two parameters were related. The peaks were attributed to individual emitters activating and subsequently being destroyed by a variety of mechanisms.

The second hypothesis was that charging of the piezoelectric transformer rapidly reduced the voltage at the output. This effect was a result of the extremely low output capacitance of the transformer (0.1−1pF). At these capacitances, even 10−100 pC of extracted charge dramatically reduced the output voltage. After 10 seconds of live-time, the output voltage was shown to drop to between 5−20 kV under worst case settings. This time frame is consistent with the measured decrease in high energy counts and is a plausible explanation for the effect.

The goal of the investigation was to determine if the piezoelectric effect could be used to make a compact x-ray source. The piezoelectric transformer demonstrated that the effect is not only able to producing high energy x-rays, but also is capable of reaching the necessary accelerating voltages for reasonable $D(d,n)^3He$ neutron production. The time-dependent drop in high energy particles is an important issue that must be solved before a steady-state piezoelectric x-ray source can be produced, however the emitter degradation and charging mechanisms offer two directions for investigating this effect.

Future Work

The electron beam optics were no longer used once the optimized configuration for x-ray production was designed. It is possible that x-ray counts could be increased further by re-incorporating the electron beam optics with the optimized configuration. A proposed configuration is diagramed in Fig. 5.1

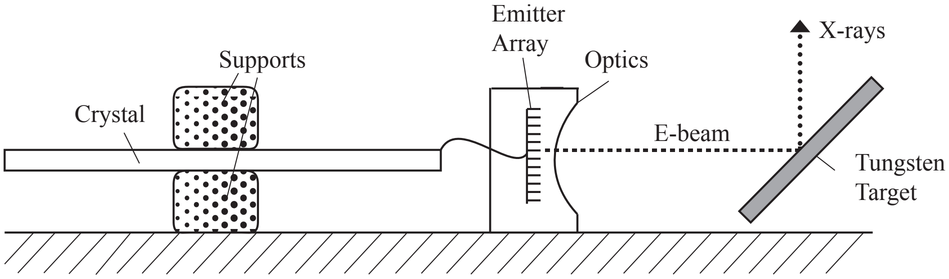

Figure 5.1: Concept of optimized configuration for electron beam optics for improved x-ray count rates

There are a number of new features included in the proposed configuration shown in Fig. 5.1. First, an off-crystal electron beam diode is implemented. In this case, rather than emitters directly attached to the transformer output, a wire is used to connect the crystal output to an array of emitters. This introduces a modular aspect to the configuration, where emitters, optics, or crystal samples can be exchanged independently of one another. This configuration also permits a simple interface to micro-fabricated emitter arrays, which could presumably produce much higher output current than the PtIr field emitters. Lastly, an angled tungsten target would absorb the focused electron beam and direct a bremsstrahlung x-ray beam to the aluminum x-ray window, permitting the use of the CdTe x-ray detector. This configuration would combine the high voltage capabilities of the optimized configuration with the focusing of the electron beam optics and could further develop the piezoelectric x-ray source.

Work should also continue on the piezoelectric plasma generator for a variety of reasons. First, the plasma generator does not use field emitters to produce electron current. For this reason, collecting time-resolved x-ray data from plasma generator and comparing to the cases of emitters would provide tremendous insight as to the nature of the time dependent decrease in counts. If the emitter degradation hypothesis is true, a steady count rate should be observed throughout the run-time. Alternatively, since no emitters are present on the plasma generator, the occurance of sharp peaks would be indicate that they are due to some effect other than emitter degradation.

It would also be possible to investigate charging effects with the plasma generator. Since the generator produces electron current from the ambient gas, it most likely would charge more slowly than the case of direct electron emission from the crystal surface. This would suggest that the plasma generator could produce x-rays for longer periods of time than the field emission x-ray source.

Finally, due to the presence of high energy deuterium ions in the plasma generator, it could be capable of producing neutrons through the $D(d,n)^3He$ reaction. A Pajarito Scientific He-3 Neutron detector is available for neutron measurements and should be used to determine if the plasma generator can produce neutrons. Results from the plasma generator experiment indicate that neutron experiments should only be run at pressures less than 10 mTorr because the output voltage was shown to drop as pressure increased beyond this point.

The optimized off-crystal electron beam diode and plasma generator are promising configurations for further developing the high voltage piezoelectric source. The electron beam diode could greatly improve upon the results acquired in this thesis by combining the focusing of the beam optics with the techniques used in the optimized configuration. Further investigation of the plasma generator could answer questions about the time-dependent decrease in x-ray counts and provide a potential means to produce neutrons.

Appendix A

Figure A.1: Data from all 58 observations made using the optimized configuration for x-ray production with a piezoelectric transformer

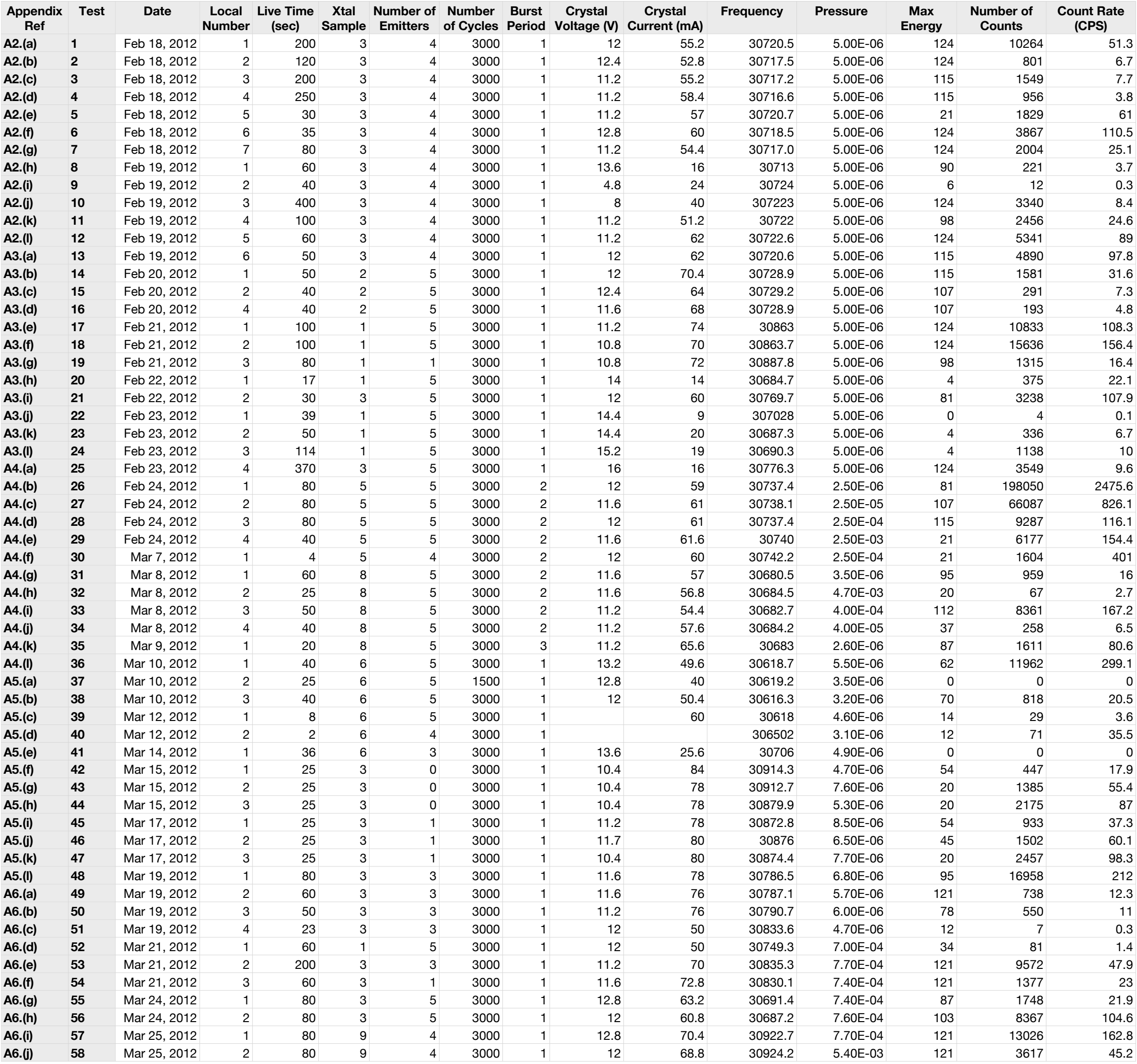

Appendix Ref	Test	Date	Local Number	Live Time (sec)	Xtal Sample	Number of Emitters	Number of Cycles	Burst Period	Crystal Voltage (V)	Crystal Current (mA)	Frequency	Pressure	Max Energy	Number of Counts	Count Rate (CPS)
A2.(a)	**1**	Feb 18, 2012	1	200	3	4	3000	1	12	55.2	30720.5	5.00E-06	124	10264	51.3
A2.(b)	**2**	Feb 18, 2012	2	120	3	4	3000	1	12.4	52.8	30717.5	5.00E-06	124	801	6.7
A2.(c)	**3**	Feb 18, 2012	3	200	3	4	3000	1	11.2	55.2	30717.2	5.00E-06	115	1549	7.7
A2.(d)	**4**	Feb 18, 2012	4	250	3	4	3000	1	11.2	58.4	30716.6	5.00E-06	115	956	3.8
A2.(e)	**5**	Feb 18, 2012	5	30	3	4	3000	1	11.2	57	30720.7	5.00E-06	21	1829	61
A2.(f)	**6**	Feb 18, 2012	6	35	3	4	3000	1	12.8	60	30718.5	5.00E-06	124	3867	110.5
A2.(g)	**7**	Feb 18, 2012	7	80	3	4	3000	1	11.2	54.4	30717.0	5.00E-06	124	2004	25.1
A2.(h)	**8**	Feb 19, 2012	1	60	3	4	3000	1	13.6	16	30713	5.00E-06	90	221	3.7
A2.(i)	**9**	Feb 19, 2012	2	40	3	4	3000	1	4.8	24	30724	5.00E-06	6	12	0.3
A2.(j)	**10**	Feb 19, 2012	3	400	3	4	3000	1	8	40	307223	5.00E-06	124	3340	8.4
A2.(k)	**11**	Feb 19, 2012	4	100	3	4	3000	1	11.2	51.2	30722	5.00E-06	98	2456	24.6
A2.(l)	**12**	Feb 19, 2012	5	60	3	4	3000	1	11.2	62	30722.6	5.00E-06	124	5341	89
A3.(a)	**13**	Feb 19, 2012	6	50	3	4	3000	1	12	62	30720.6	5.00E-06	115	4890	97.8
A3.(b)	**14**	Feb 20, 2012	1	50	2	5	3000	1	12	70.4	30728.9	5.00E-06	115	1581	31.6
A3.(c)	**15**	Feb 20, 2012	2	40	2	5	3000	1	12.4	64	30729.2	5.00E-06	107	291	7.3
A3.(d)	**16**	Feb 20, 2012	4	40	2	5	3000	1	11.6	68	30728.9	5.00E-06	107	193	4.8
A3.(e)	**17**	Feb 21, 2012	1	100	1	5	3000	1	11.2	74	30863	5.00E-06	124	10833	108.3
A3.(f)	**18**	Feb 21, 2012	2	100	1	5	3000	1	10.8	70	30863.7	5.00E-06	124	15636	156.4
A3.(g)	**19**	Feb 21, 2012	3	80	1	1	3000	1	10.8	72	30887.8	5.00E-06	98	1315	16.4
A3.(h)	**20**	Feb 22, 2012	1	17	1	5	3000	1	14	14	30684.7	5.00E-06	4	375	22.1
A3.(i)	**21**	Feb 22, 2012	2	30	3	5	3000	1	12	60	30769.7	5.00E-06	81	3238	107.9
A3.(j)	**22**	Feb 23, 2012	1	39	1	5	3000	1	14.4	9	307028	5.00E-06	0	4	0.1
A3.(k)	**23**	Feb 23, 2012	2	50	1	5	3000	1	14.4	20	30687.3	5.00E-06	4	336	6.7
A3.(l)	**24**	Feb 23, 2012	3	114	1	5	3000	1	15.2	19	30690.3	5.00E-06	4	1138	10
A4.(a)	**25**	Feb 23, 2012	4	370	3	5	3000	1	16	16	30776.3	5.00E-06	124	3549	9.6
A4.(b)	**26**	Feb 24, 2012	1	80	5	5	3000	2	12	59	30737.4	2.50E-06	81	198050	2475.6
A4.(c)	**27**	Feb 24, 2012	2	80	5	5	3000	2	11.6	61	30738.1	2.50E-05	107	66087	826.1
A4.(d)	**28**	Feb 24, 2012	3	80	5	5	3000	2	12	61	30737.4	2.50E-04	115	9287	116.1
A4.(e)	**29**	Feb 24, 2012	4	40	5	5	3000	2	11.6	61.6	30740	2.50E-03	21	6177	154.4
A4.(f)	**30**	Mar 7, 2012	1	4	5	4	3000	2	12	60	30742.2	2.50E-04	21	1604	401
A4.(g)	**31**	Mar 8, 2012	1	60	8	5	3000	2	11.6	57	30680.5	3.50E-06	95	959	16
A4.(h)	**32**	Mar 8, 2012	2	25	8	5	3000	2	11.6	56.8	30684.5	4.70E-03	20	67	2.7
A4.(i)	**33**	Mar 8, 2012	3	50	8	5	3000	2	11.2	54.4	30682.7	4.00E-04	112	8361	167.2
A4.(j)	**34**	Mar 8, 2012	4	40	8	5	3000	2	11.2	57.6	30684.2	4.00E-05	37	258	6.5
A4.(k)	**35**	Mar 9, 2012	1	20	8	5	3000	3	11.2	65.6	30683	2.60E-06	87	1611	80.6
A4.(l)	**36**	Mar 10, 2012	1	40	6	5	3000	1	13.2	49.6	30618.7	5.50E-06	62	11962	299.1
A5.(a)	**37**	Mar 10, 2012	2	25	6	5	1500	1	12.8	40	30619.2	3.50E-06	0	0	0
A5.(b)	**38**	Mar 10, 2012	3	40	6	5	3000	1	12	50.4	30616.3	3.20E-06	70	818	20.5
A5.(c)	**39**	Mar 12, 2012	1	8	6	5	3000	1		60	30618	4.60E-06	14	29	3.6
A5.(d)	**40**	Mar 12, 2012	2	2	6	4	3000	1			306502	3.10E-06	12	71	35.5
A5.(e)	**41**	Mar 14, 2012	1	36	6	3	3000	1	13.6	25.6	30706	4.90E-06	0	0	0
A5.(f)	**42**	Mar 15, 2012	1	25	3	0	3000	1	10.4	84	30914.3	4.70E-06	54	447	17.9
A5.(g)	**43**	Mar 15, 2012	2	25	3	0	3000	1	10.4	78	30912.7	7.60E-06	20	1385	55.4
A5.(h)	**44**	Mar 15, 2012	3	25	3	0	3000	1	10.4	78	30879.9	5.30E-06	20	2175	87
A5.(i)	**45**	Mar 17, 2012	1	25	3	1	3000	1	11.2	78	30872.8	8.50E-06	54	933	37.3
A5.(j)	**46**	Mar 17, 2012	2	25	3	1	3000	1	11.7	80	30876	6.50E-06	45	1502	60.1
A5.(k)	**47**	Mar 17, 2012	3	25	3	1	3000	1	10.4	80	30874.4	7.70E-06	20	2457	98.3
A5.(l)	**48**	Mar 19, 2012	1	80	3	3	3000	1	11.6	78	30786.5	6.80E-06	95	16958	212
A6.(a)	**49**	Mar 19, 2012	2	60	3	3	3000	1	11.6	76	30787.1	5.70E-06	121	738	12.3
A6.(b)	**50**	Mar 19, 2012	3	50	3	3	3000	1	11.2	76	30790.7	6.00E-06	78	550	11
A6.(c)	**51**	Mar 19, 2012	4	23	3	3	3000	1	12	50	30833.6	4.70E-06	12	7	0.3
A6.(d)	**52**	Mar 21, 2012	1	60	1	5	3000	1	12	50	30749.3	7.00E-04	34	81	1.4
A6.(e)	**53**	Mar 21, 2012	2	200	3	3	3000	1	11.2	70	30835.3	7.70E-04	121	9572	47.9
A6.(f)	**54**	Mar 21, 2012	3	60	3	1	3000	1	11.6	72.8	30830.1	7.40E-04	121	1377	23
A6.(g)	**55**	Mar 24, 2012	1	80	3	5	3000	1	12.8	63.2	30691.4	7.40E-04	87	1748	21.9
A6.(h)	**56**	Mar 24, 2012	2	80	3	5	3000	1	12	60.8	30687.2	7.60E-04	103	8367	104.6
A6.(i)	**57**	Mar 25, 2012	1	80	9	4	3000	1	12.8	70.4	30922.7	7.70E-04	121	13026	162.8
A6.(j)	**58**	Mar 25, 2012	2	80	9	4	3000	1	12	68.8	30924.2	5.40E-03	121	3617	45.2

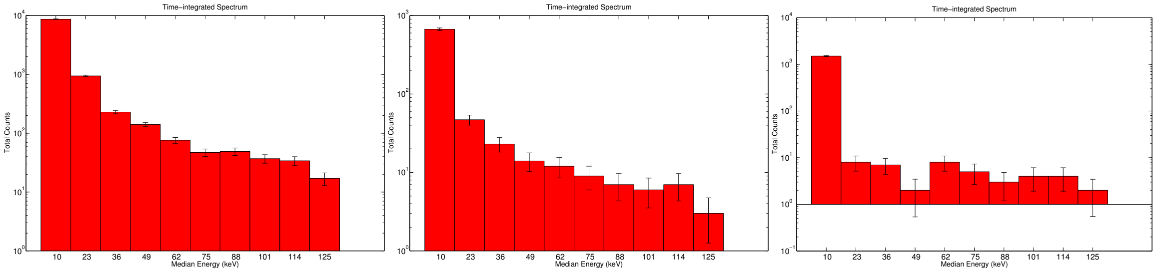

(a) Test 1 (b) Test 2 (c) Test 3

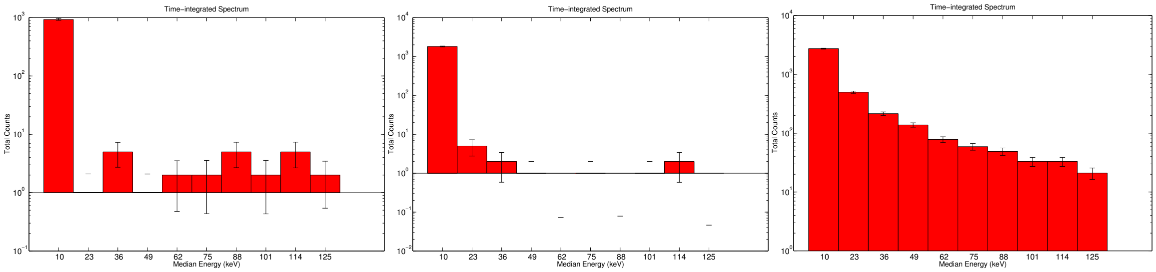

(d) Test 4 (e) Test 5 (f) Test 6

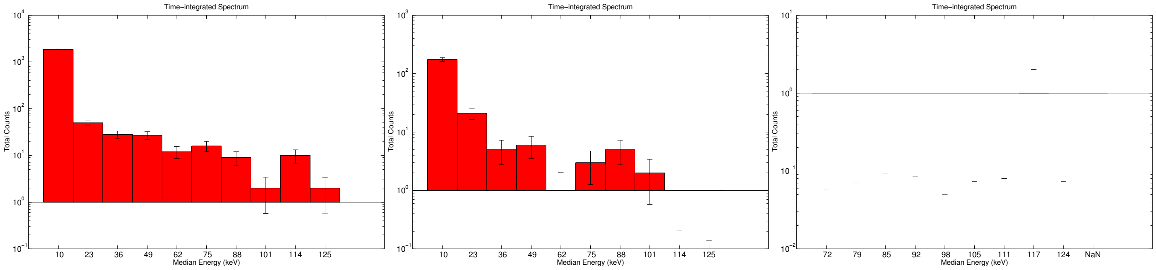

(g) Test 7 (h) Test 8 (i) Test 9

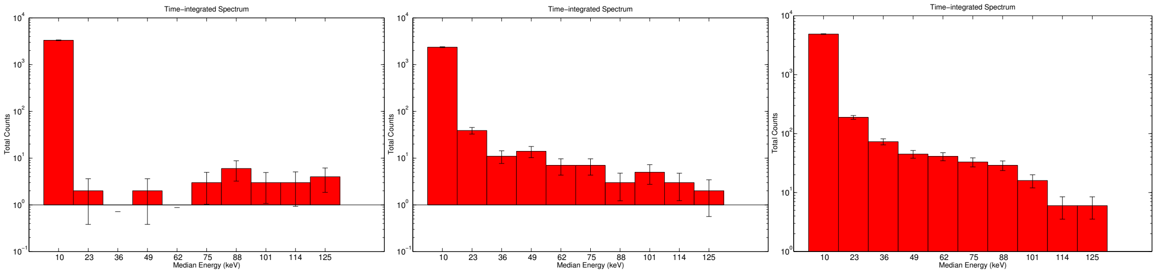

(j) Test 10 (k) Test 11 (l) Test 12

Figure A.2: Tests 1−12

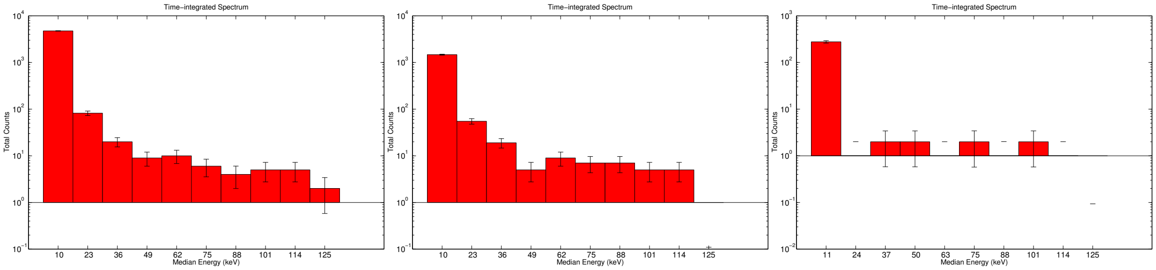

(a) Test 13 (b) Test 14 (c) Test 15

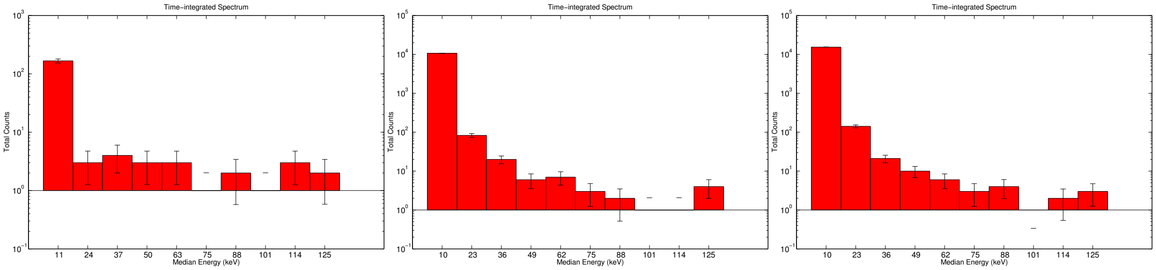

(d) Test 16 (e) Test 17 (f) Test 18

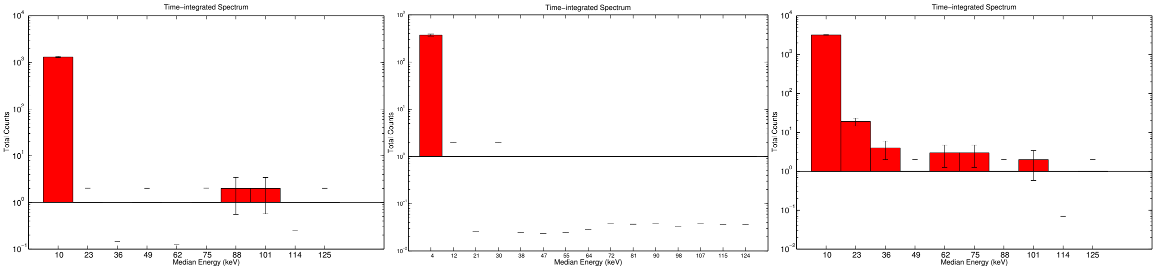

(g) Test 19 (h) Test 20 (i) Test 21

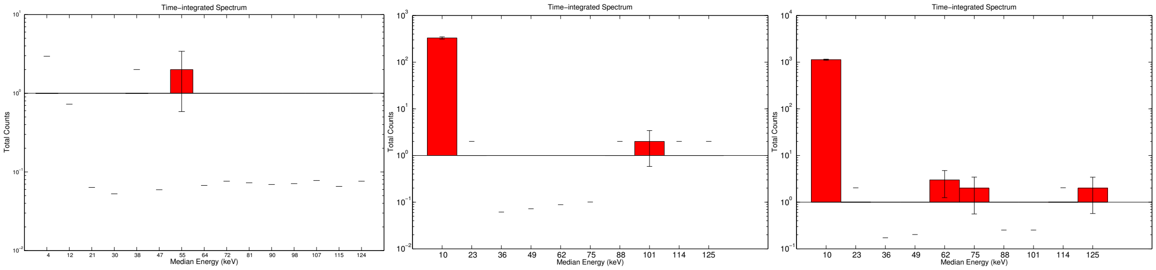

(j) Test 22 (k) Test 23 (l) Test 24

Figure A.3: Tests 13−24

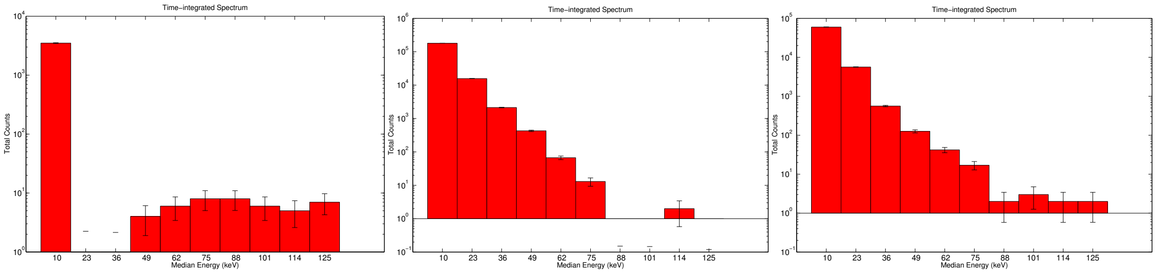

(a) Test 25 (b) Test 26 (c) Test 27

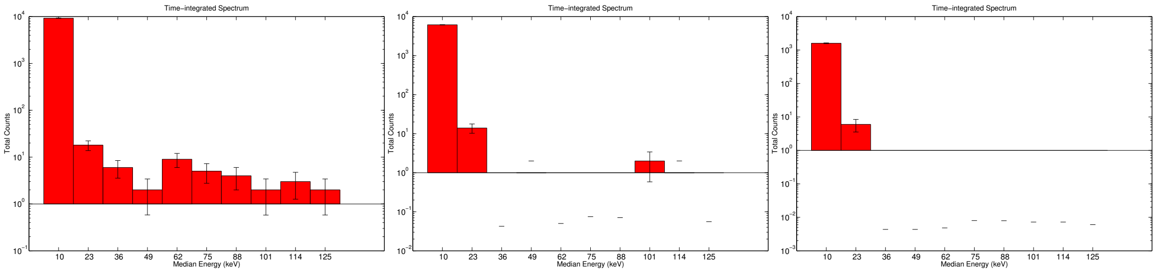

(d) Test 28 (e) Test 29 (f) Test 30

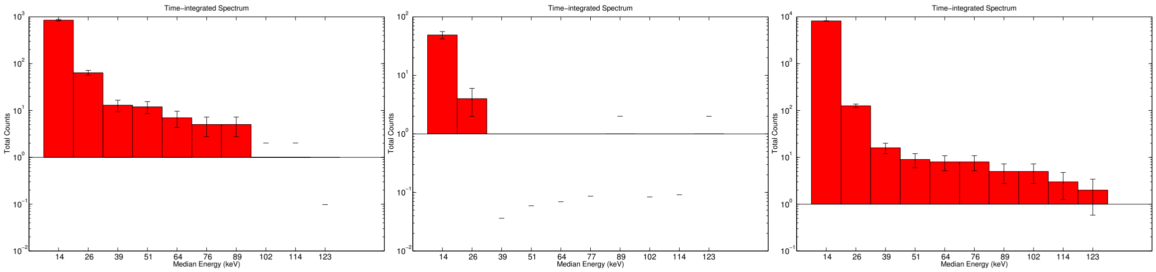

(g) Test 31 (h) Test 32 (i) Test 33

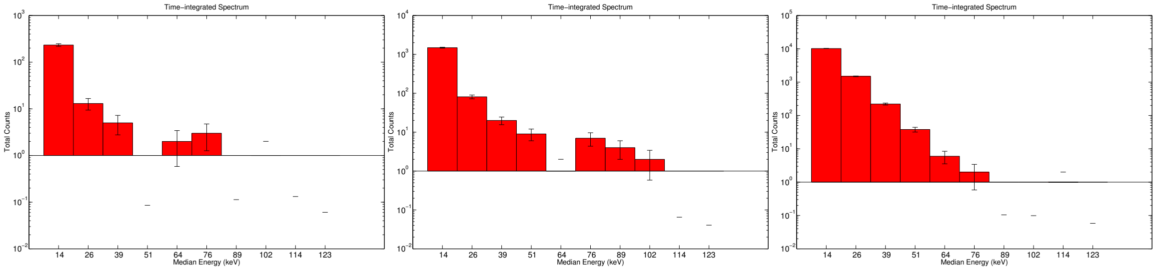

(j) Test 34 (k) Test 35 (l) Test 36

Figure A.4: Tests 25−36

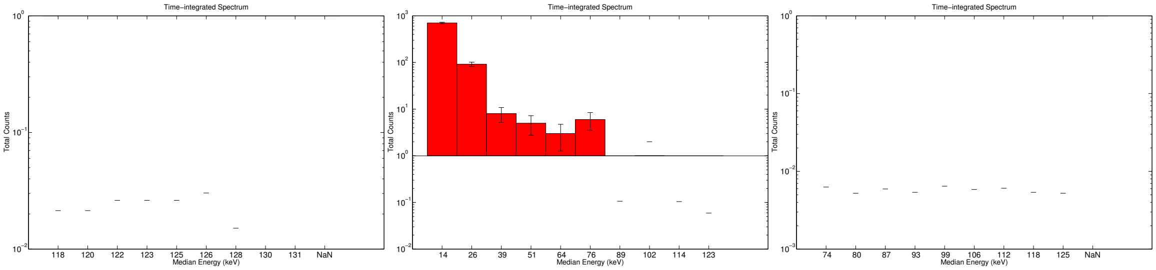

(a) Test 37 (b) Test 38 (c) Test 39

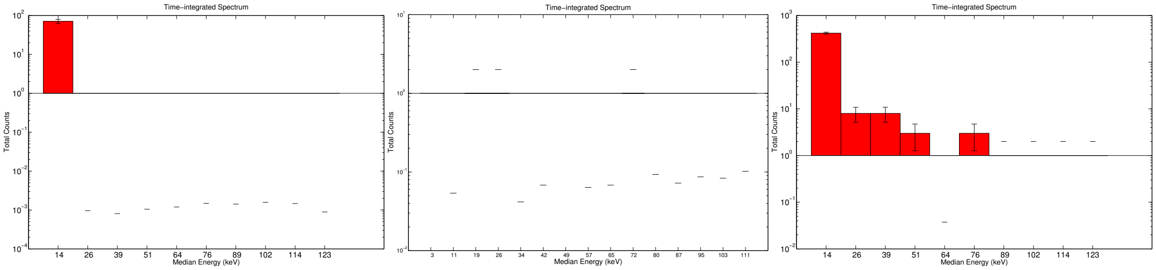

(d) Test 40 (e) Test 41 (f) Test 42

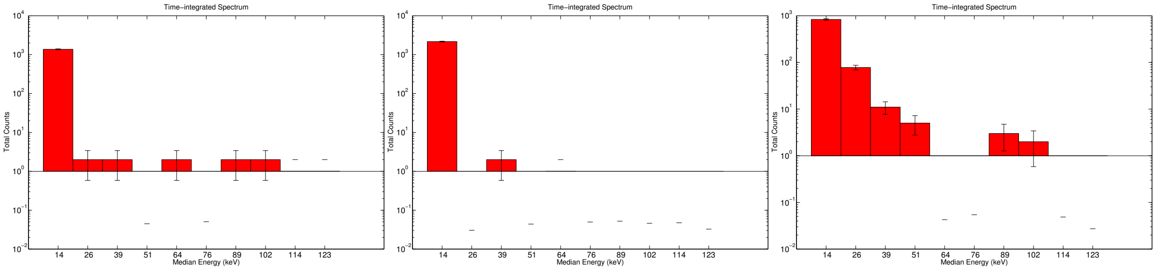

(g) Test 43 (h) Test 44 (i) Test 45

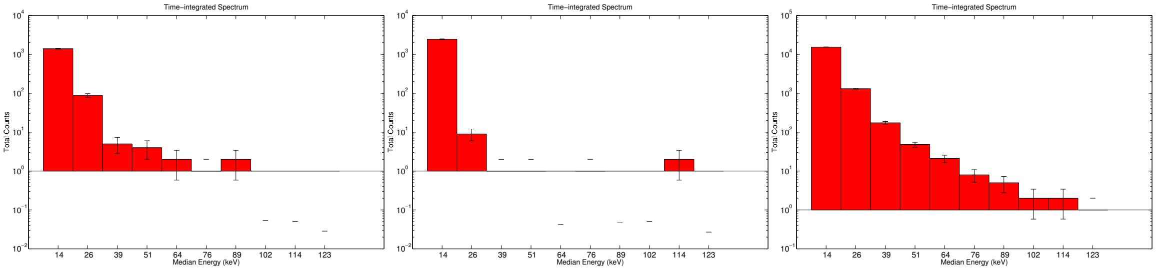

(j) Test 46 (k) Test 47 (l) Test 48

Figure A.5: Tests 37−48

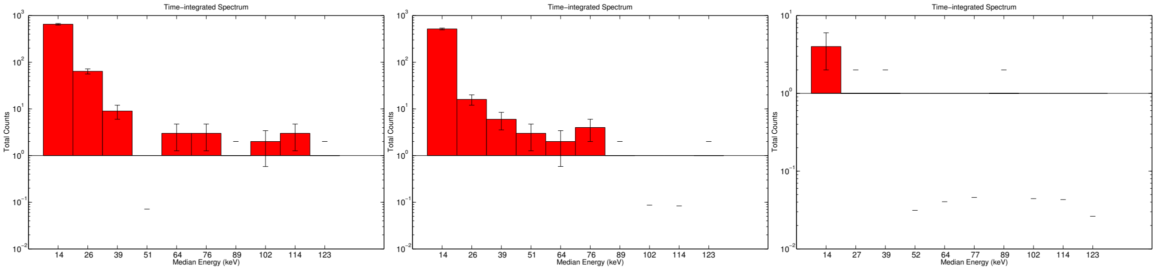

(a) Test 49 (b) Test 50 (c) Test 51

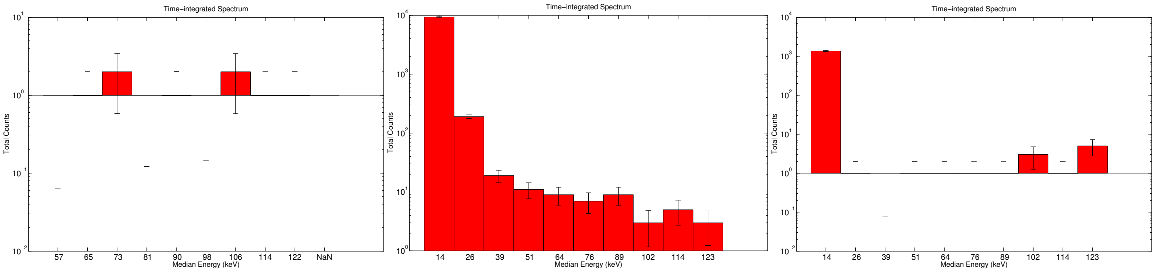

(d) Test 52 (e) Test 53 (f) Test 54

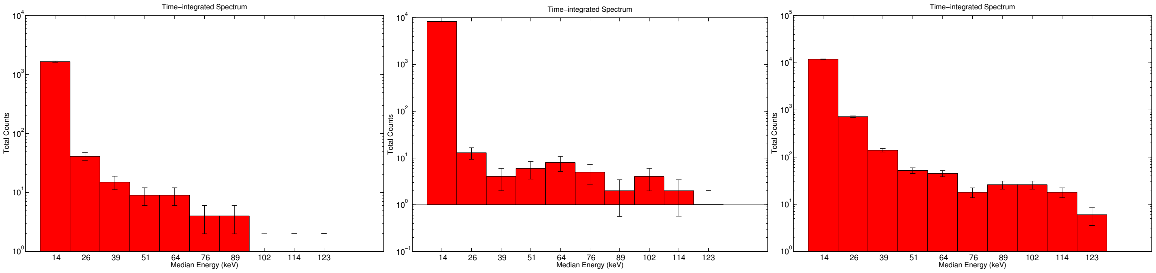

(g) Test 55 (h) Test 56 (i) Test 57

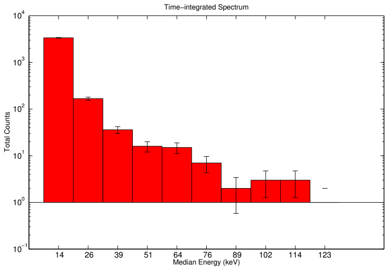

(j) Test 58

Figure A.6: Tests 49−58

Bibliography

[1] R. Talman, *Accelerator X-Ray Sources.* Wiley-VCH, 2006.

[2] J. B. Murphy, "X-ray lithography sources: A reivew," in *Particle Accelerator Conferenece*, (Chicago, IL), Brookhaven National Laboratory, 1989.

[3] F. Pfeiffer, "Hard x-ray phase tomography with low-brilliance sources," *Physical Review Letter*, vol. 98, 2007.

[4] "Quasi-monochromatic flash x-ray generator utilizing disk-cathode molybdenum tube," *Sato, E and Michiaki, S and Tanaka, E and Hayasi, Y and Germer, R and Mori, H and Kawai, T and Ichimaru, T, and Sato, S and Takayama, K and Ido, H*, vol. 43, no. 10, pp. 7324–7328, 2004.

[5] J. A. Geuther and Y. Danon, "High-energy x-ray production with pyroelectric crystals," *Journal of Applied Physics*, vol. 97, May 2005.

[6] W. Tornow, S. Lynam, and S. Shafroth, "Substantial increase in acceleration potential of pyroelectric crystals," *Journal of Applied Physics*, vol. 107, no. 6, 2010.

[7] J. Hird, "A triboelectric x-ray source," *Applied Physics Letters*, vol. 98, March 2011.

[8] A. Benwell, S. Kovaleski, and M. Kemp, "A resonantly driven piezoelectric transformer for high voltage generation," in *IEEE International Power Modulators and High Voltage Conference, Proceedings of the 2008*, pp. 113 –116, may 2008.

[9] A. L. Benwell, *A high voltage piezoelectric transformer for active interrogation.* PhD thesis, Univeristy of Missouri, 2009.

[10] International Workshop on Micro and Nanotechnology for Power Generation and Energy Conversion Applications, *Ultra-Compact Piezoelectric Transformer Charged Particle Acceleration*, (Washington, DC), Dec. 2009.

[11] J. Yang, "Piezoelectric transformer structural modeling - a review," *Ultrasonics, Ferroelectrics and Frequency Control, IEEE Transactions on*, vol. 54, pp. 1154 –1170, june 2007.

[12] L. Hwang, J. Yoo, E. Jang, D. Oh, Y. Jeong, I. Ahn, and M. Cho, "Fabrication and characteristics of pda lcd backlight driving circuits using piezoelectric transformer," *Sensors and Actuators*, 2004.

[13] P. Bolhuis, "Gas discharge flas lamp with piezoelectric trigger generator," *United States Patent*, 1978.

[14] Y. Park, "Electrical properties of a piezoelectric transformer for an ac-dc converter," *Journal of the Korean Physical Society*, vol. 57, pp. 1131–1133, October 2010.

[15] H. Itoh, K. Teranishi, and S. Suzuki, "Discharge plasmas generated by piezoelectric transformers and their applications," *Plasma Sources Science and Technology*, vol. 15, no. 2, p. S51, 2006.

[16] T. I. of Electrical and I. Electronics Engineers, "Ieee standard on piezoelectricity." Standards Committee of the IEEE Ultrasonics, Ferroelectrics, and Frequency Control Society, March 1987.

[17] K. Nakamura and Y. Adachi, "Piezoelectric transformers using linbo3 single crystals," *Electronics and Communications in Japan (Part III: Fundamental Electronic Science)*, vol. 81, no. 7, pp. 1–6, 1998.

[18] J. Yang and X. Zhang, "Extensional vibration of a nonuniform piezoceramic rod and high voltage generation," *International Journal of Applied Electromagnetics and Mechanics*, vol. 16, pp. 29–42, January 2002.

[19] C. A. Rosen, "Electromechanical transducer." United States Patent Office, Apr 1958.

[20] C. A. Rosen, "Electrical conversion apparatus." United States Patent Office, Nov 1956.

[21] R. W. T. Gaylord, "Lithium niobate: Summary of physical properies and crystal structure," *Applied Physics A*, vol. 37, pp. 191–203, March 1985.

[22] A. Howatson, *An Introduction to Gas Discharges.* Pergamon Press, 1965.

[23] R. Gomer, *Field Emission and Field Ionization.* No. 9 in Harvard Monographs in Applied Science, Cambridge, MA: Harvard University Press, 1961.

[24] N. de Jonge and J.-M. Bonard, "Carbon nanotube electron sources and applications," *Philosophical Transactions of the Royal Society of London*, vol. 362, no. 1823, pp. 2239–2266, 2004.

[25] C. Edgecombe and U. Valdrè, "Microscopy and computational modelling to elucidate the enhancement factor for field electron emitters," *Journal of Microscopy*, vol. 203, pp. 188–194, August 2000.

[26] W. Dyke and W. Dolan, "Field emission," *Adv. Electronics and Electron Phys.*, vol. 8, pp. 90–187, 1956.

[27] U. V. Richard Forbes, C.J. Edgcombe, "Some comments on modesl for field enhancement," *Ultramicroscopy*, vol. 95, pp. 57–65, 2003.

[28] R. D. Evans, *The Atomic Nucleus.* International Series in Pure and Applied Physics, McGraw-Hill Book Company, 1955.

[29] N. Tsoulfanidis, *Measurement and Detection of Radiation.* Taylor and Francis, 2 ed., March 1995.

[30] Atzeni, "Nuclear fusion reactions." Oxford University Press, April 2004.

[31] G. Miley, H. Towner, and N. Ivich, "Fusion cross section and reactivities," Tech. Rep. COO-2218-17, University of Illinois, Urbana, IL, 1974.

[32] B. Duane, *Fusion Cross Section Theory.* Brookhaven National Laboratory, 1972.

[33] M. Prelas and M. Peck, *Nonproliferation Issues for Weapons of Mass Destruction.* Taylor and Francis, 2005.

[34] T. Ghosh, M. Prelas, D. Viswanath, and S. Loyalka, *Science and Technology of Terrorism and Counterterrorism.* Marcel Dekker, 2002.

[35] C. Moss, C. Hollas, G. McKinney, and W. Meyers, "Comparison of active interrogation techniques," *IEEE Transactions on Nuclear Science*, vol. 53, pp. 2242–2246, August 2006.

[36] C. Moss, C. Hollas, and W. Meyers, "Active interrogation of highly enriched uranium," (Guildford, UK), 11th Internation Conference Modern Trends in Activation Analysis, 2004.

[37] J. Mihalczo, "Radiation detection for active interrogation of heu," tech. rep., Oak Ridge National Laboritory, Oak Ridge, Tennessee, Dec. 2004.

[38] T. M. Miller and B. W. Patton, "Investigations of active interrogation techniques to detect special nuclear material in maritime environments," tech. rep., Oak Ridge National Laboratory, P.O. Box 2008, MS-6170, Oak Ridge, TN 37831, USA.

[39] C. Moss, M. Brener, C. Hollas, and W. Meyers, "Portable active interrogation system," *Nuclear Instruments and Methods in Physics Research*, pp. 793–797, Aug 2005.

[40] "Comsol multiphysics."

[41] K. K. Wong, *Properties of Lithium Niobate.* Northstar Photonics, Inc, 2002.

[42] C. Bai, *Scanning Tunneling Microscopy and Its Applications.* Shanghai : Scientific & Technical Publishers, seconds, revised ed., 1995.

[43] H. Jaffe and D. Berlincourt, "Piezoelectric transducer materials," *Proceedings of the IEEE*, vol. 53, pp. 1372 – 1386, oct. 1965.

[44] R. Redus, *Efficiency of XR-100T-CdTe Detectors Application Note (AN-CdTe-001 Rev. 1).* Amptek, Inc., http://amptek.com/anczt1.html.

[45] *http://www.nanoscience.com/store/pc/viewPrd.asp?idproduct=149.* nanoScience Instruments, June 2012.

[46] J. A. VanGordon, B. Gall, P. Norgard, S. Kovaleski, E. Baxter, B. Kim, J. Kwon, and G. Dale, "Effects of capacitive versus resistive loading on high transformation ratio piezoelectric transformers for modular design considerations." 2012 IEEE International High Voltage and Power Modulator Conference, June 2012.

[47] MathWorks, "Matlab."

[48] A. J. L. Michael A Lieberman, *Principles of Plasma Discharges and Materials Processing.* Wiley-Interscience, second ed., 2005.

[49] F. Llewellyn-Jones, *The Glow Discharge.* Methuen's Physical Monographs, 1966.

[50] F. Chen, *Introduction to Plasma Physics and Controlled Fusion*, vol. 1: Plasma Physics. Plenum Press, second edition ed., 1984.